

OCH3R: Object-Centric Holistic 3D Reconstruction

Yi Du Yang You Xiang Wan Leonidas Guibas
Stanford University
{duyi, yangyou, oscarwan, guibas}@stanford.edu

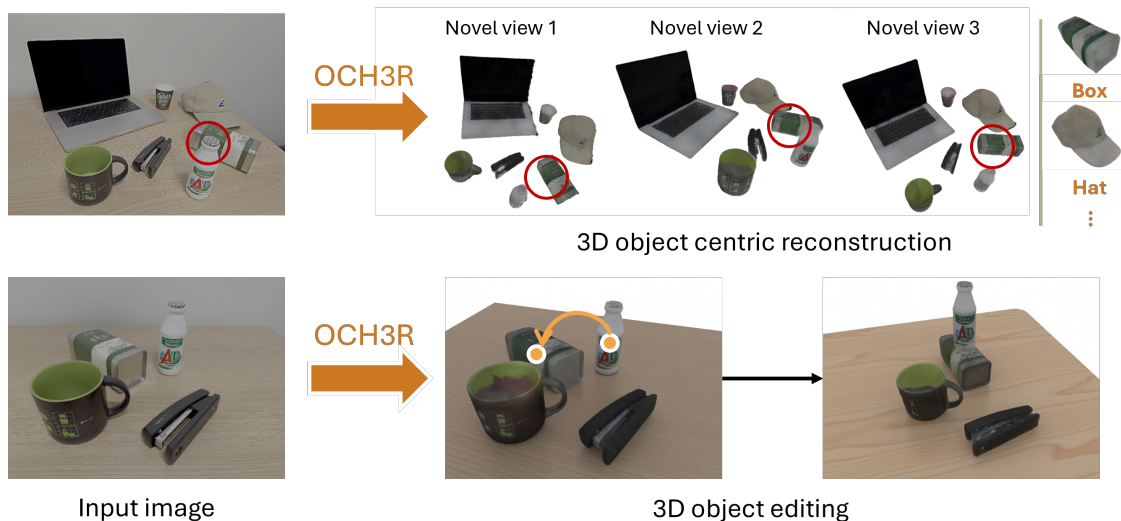


Figure 1. **OCH3R enables fully object-centric 3D scene reconstruction from a single RGB image.** Given one input view, OCH3R discovers all object instances, predicts their 6D poses, and reconstructs each object as a manipulable 3D Gaussian model in a single forward pass. Our feed-forward, per-pixel prediction framework supports selecting, moving, and rendering objects from arbitrary novel views without external segmentors or multi-stage pipelines. OCH3R produces amodally complete, editable 3D objects and generalizes to cluttered real scenes, enabling downstream tasks such as rearrangement and AR editing. The red circles highlight occluded regions that OCH3R successfully completes in 3D.

Abstract

Object-centric scene understanding is a fundamental challenge in computer vision. Existing approaches often rely on multi-stage pipelines that first apply pre-trained segmentors to extract individual objects, followed by per-object 3D reconstruction. Such methods are computationally expensive, fragile to segmentation errors, and scale poorly with scene complexity. We introduce **OCH3R**, a unified framework for **Object-Centric Holistic 3D Reconstruction** from a single RGB image. OCH3R performs one forward pass to simultaneously predict all object instances with their 6D poses and detailed 3D reconstructions. The key idea is a transformer architecture that predicts per-pixel attributes, including CLIP-based category embeddings, metric depth, normalized object coordinates (NOCS), and a fixed number of 3D Gaussians representing each object. To supervise these Gaussian reconstructions, we transform

them into canonical space using the predicted 6D poses and align them with pre-rendered canonical ground truth, avoiding costly per-image Gaussian label generation. On standard indoor benchmarks, OCH3R achieves state-of-the-art performance across monocular depth estimation, open-vocabulary semantic segmentation, and RGB-only category-level 6D pose estimation, while producing high-fidelity, editable per-object reconstructions. Crucially, inference is fully feed-forward and scales independently of the number of objects, offering orders-of-magnitude speedups over conventional multi-stage pipelines in cluttered scenes.

1. Introduction

Understanding a scene as a composition of discrete, posed objects from a single image is a long-standing goal in computer vision. Many downstream applications including robotic manipulation, AR editing, and simulation rely on

object-centric outputs [73], where each object is represented with geometry, pose, and semantics that can be selected or manipulated. We study the following problem: given a single RGB image of an indoor tabletop scene, recover all objects together with their 6D poses and corresponding 3D Gaussians in one forward pass.

Prior work largely falls into two groups. Scene-level, feed-forward methods (*e.g.*, one-pass Gaussian predictors) [5, 54, 68, 74, 82] are fast and photorealistic, but typically produce an undifferentiated “soup” of geometry without instance-level structure, canonical frames, or object poses. Object-level approaches [24, 25, 73] instead rely on multi-stage pipelines that begin with external open-vocabulary segmentors and then perform per-object reconstruction, alignment, and correction. These systems often depend on RGB-D inputs or category-specific priors, and they are fragile to upstream errors, difficult to scale with the number of objects, and not trained end-to-end. As a result, their robustness and accuracy degrade in cluttered tabletop scenes.

To address these limitations, we introduce **OCH3R**, a unified, object-centric, holistic 3D reconstructor that converts a single RGB image into a set of posed 3D objects in one pass. The key in our design is a 48-layer transformer that predicts dense, pixel-aligned attributes: CLIP [45]-based category embeddings, metric depth, normalized object coordinates (NOCS) [62], and a small set of 3D Gaussians [29] per pixel. During inference, object instances and their poses are recovered by clustering the semantic embeddings and estimating each object’s SIM(3) pose using the predicted NOCS field.

To train the Gaussian representation, we allow Gaussians at each pixel to move freely off the pixel rays to compensate for (self-) occlusion. Rather than supervising Gaussians per training image [52, 53], we adopt Canonical-Space Supervision: per-object Gaussians are transformed into canonical space using its SIM(3) pose, and their renderings are optimized against pre-rendered ground truth in the canonical frame. This eliminates the need for costly per-image Gaussian labels and promotes amodal shape completion.

We train on a curated, large-scale dataset that integrates PACE [75], Omni6DPose [81], GSO [12], and HyperSim [48], offering broad coverage across object categories, poses, and occlusion patterns.

Our experiments show that OCH3R substantially outperforms previous baselines across all evaluated tabletop object-centric benchmarks. OCH3R delivers consistently higher geometric accuracy, better semantic alignment, and significantly more complete amodal reconstructions. Importantly, because OCH3R reconstructs all objects in a single forward pass, it achieves orders-of-magnitude faster inference than multi-stage pipelines while avoiding their brittleness to segmentation or pose-estimation errors. Together,

these results highlight the effectiveness of our unified formulation and its practical advantages for real-world object-centric applications.

To summarize, our contributions are as follows:

1. We construct a large scale dataset for holistic object centric 3D scene representation. We assemble, relabel, and align PACE [75], Omni6DPose [81], GSO [12], and HyperSim [48] into a unified dataset designed for object centric 3D tasks, providing per instance masks, segmentation labels, SIM(3) poses, and 3D models.
2. We propose a model that yields high-fidelity 3D reconstructions, recovering fine-grained geometry and amodal structure, while jointly predicting semantics, monocular depth, and object poses in a single pass.
3. Experiments show that our model reconstructs real-world tabletop scenes with arbitrary numbers of objects, delivering more photorealistic and amodally complete results while running far faster than multi-stage pipelines.

2. Related Work

Feed-forward 3D reconstruction. Feed-forward 3D reconstruction maps one or a few images directly to a renderable 3D scene. Previous works have explored 3D representations including voxel grids [57, 58], multi-plane images [35, 59], meshes [17, 18], surfel [16], and radiance fields [21, 76]. More recently, 3D Gaussians [30] have emerged as a dominant representation for feed-forward regression thanks to their real-time differentiable rendering and compatibility with high-capacity 2D backbones.

Early feed-forward Gaussian predictors focus on single, centered objects, assigning one Gaussian to each input pixel and directly regressing its parameters without test-time optimization [52, 55, 71, 80]. These models deliver fast and high-quality reconstructions, but they assume clean, uncluttered inputs and cannot handle occlusions, multiple instances, or reassemble per-object predictions into a scene.

In contrast, scene-level Gaussian models predict a dense Gaussian field for an entire scene from one [53] or multiple images [5, 8, 65, 68, 74, 82]. Techniques including probabilistic splatting [5], cost-volume aggregation [8], depth conditioning [68], pose-free formulations [74] and large transformer backbones [82] have been explored to improve performance. While effective for novel-view synthesis, these scene-level approaches treat the world as a single undifferentiated cloud without instance decomposition, preventing downstream reasoning or interaction.

Object-centric scene reconstruction. A separate line of work performs object-centric scene reconstruction, explicitly recovering a set of 3D object instances and their layout. IM2CAD [26], Total3DUnderstanding [41], Zhang *et al.* [79], and CoReNet [44] reconstruct indoor scenes from

a single image by detecting furniture and room layout, then retrieving or predicting per-object geometry and enforcing consistency in a shared 3D frame. CAD- and RGB-D-based pipelines such as Mask2CAD [32], ROCA [19], CenterSnap [24], and ShAPO [25] further combine instance detection and depth with CAD retrieval or learned latent shape codes for each object, making them sensitive to upstream errors and computationally costly as the number of objects increases.

More recent methods introduce strong generative priors but largely retain this compositional, multi-stage design: Gen3DSR [1], CAST [73], and DepR [83] first apply monocular depth estimation and instance segmentation, then run object-level image-to-3D or diffusion models and compose the resulting objects into a coherent scene; MIDI [23] extends pre-trained image-to-3D generators to a multi-instance diffusion model that still takes segmented object crops as input. Consequently, computational cost and brittleness scale with the number and quality of segmented instances. With a sufficiently large dataset and a sufficiently powerful model, we show that single-view, object-aware 3D reconstruction can be approached as a direct, feed-forward prediction problem, rather than a fragile sequence of segmentation, retrieval, optimization, or generative refinement. In practice, this shift yields reconstructions that are not only orders-of-magnitude faster but also higher-fidelity.

3. Preliminaries

3D Gaussian Splatting. Gaussian Splatting [30] renders a scene represented by a finite set of anisotropic 3D Gaussian primitives by projecting each primitive to the image plane as a 2D Gaussian and alpha-compositing them in visibility order, yielding a fast, differentiable approximation to emission-absorption volume rendering. Compared with ray-sampled neural fields [40], splatting enables real-time rendering and efficient gradient backpropagation, and is widely used as the rendering backbone in recent feed-forward reconstruction methods [5, 6, 8, 52, 54, 55, 65, 71, 74, 82]; we adopt the same renderer throughout.

Normalized Object Coordinate Space. Normalized Object Coordinate Space (NOCS) [63] assigns each 3D point on an object instance a category-level, pose-invariant coordinate $\mathbf{c} \in [0, 1]^3$ within a unit canonical cube whose axes are consistently aligned across instances of that category. We denote this unit cube as the *canonical space* and to its associated rigid coordinate system as the *canonical frame*.

Dense per-pixel NOCS predictions $\hat{\mathbf{c}}_{u,v}$ provide pixel-to-canonical correspondences that, together with the predicted 3D point map, are sufficient to recover an instance’s category-level pose $\Pi = (s, R, \mathbf{t}) \in \text{SIM}(3)$ (Sec. 4.2). By definition, Π transforms canonical coordinates to the camera (or scene) frame: $\mathbf{x}^{\text{cam}} = \Pi(\mathbf{x}^{\text{can}}) = sR\mathbf{x}^{\text{can}} + \mathbf{t}$, with

inverse mapping given by $\Pi^{-1}(\mathbf{x}^{\text{cam}}) = s^{-1}R^\top \cdot (\mathbf{x}^{\text{cam}} - \mathbf{t})$.

4. Method

4.1. Problem formulation and notation

Given a single RGB image $I \in \mathbb{R}^{H \times W \times 3}$ with unknown intrinsics K , OCH3R converts the image into an object-centric scene: a set of instances, each with a category-level $\text{SIM}(3)$ pose and a high-fidelity 3D representation. Achieving this in one pass requires pixel-aligned predictions that are sufficient to (i) discover instances and semantics, (ii) recover a metric similarity transform for each object, and (iii) assemble amodally complete Gaussian representation of each object into an interactive scene.

Specifically, for each pixel (u, v) , our network Φ outputs:

$$\Phi(I)_{u,v} = (\hat{\mathbf{e}}_{u,v}, \hat{d}_{u,v}, \hat{\mathbf{c}}_{u,v}, \hat{\mathcal{G}}_{u,v}), \quad (1)$$

where $\hat{\mathbf{e}}_{u,v} \in \mathbb{R}^{512}$ is the semantic label of the object that this pixel belongs to. We define semantic label of an object as the CLIP [45] embedding of the object’s category name [34]. $\hat{d}_{u,v} \in \mathbb{R}^+$ is the predicted metric depth. It enables back-projecting the pixel into 3D space via $\hat{\mathbf{p}}_{u,v} = \hat{d}_{u,v} \cdot K^{-1} [u \ v \ 1]^\top \in \mathbb{R}^3$. $\hat{\mathbf{c}}_{u,v} \in [0, 1]^3$ is the predicted NOCS [63] coordinate, which enables $\text{SIM}(3)$ pose recovery.

$\hat{\mathcal{G}}_{u,v} = \{g_{u,v}^{(i)}\}_{i=1}^k$ is a small set of anisotropic 3D Gaussian primitives (we use $k = 2$) that will be aggregated into per-object reconstruction:

$$g_{u,v}^{(i)} = (\boldsymbol{\mu}_{u,v}^{(i)}, \Sigma_{u,v}^{(i)}, \alpha_{u,v}^{(i)}, \mathbf{S}_{u,v}^{(i)}), \quad (2)$$

with mean $\boldsymbol{\mu}_{u,v}^{(i)} \in \mathbb{R}^3$, covariance $\Sigma_{u,v}^{(i)} \in \mathbb{S}_{++}^3$, opacity $\alpha_{u,v}^{(i)} \in (0, 1)$, and RGB spherical harmonics (SH) coefficients $\mathbf{S}_{u,v}^{(i)} \in \mathbb{R}^{3(L+1)^2}$ (order L). The Gaussian parameters are defined and predicted in camera frame, and will be transformed into each object’s canonical frame for supervision and inference (Sec. 4.3).

Following VGGT [64], we also predict the camera field of view $(\hat{\theta}_w, \hat{\theta}_h)$ of the input image and construct K with $f_w = \frac{W}{2 \tan(\hat{\theta}_w/2)}$, $f_h = \frac{H}{2 \tan(\hat{\theta}_h/2)}$ and principal point at image center.

In Sec. 4.2, we show how $\hat{\mathbf{e}}$, \hat{d} , $\hat{\mathbf{c}}$, and $\hat{\mathcal{G}}$ are used to discover instances, estimate object poses, and assemble reconstructed objects. Sec. 4.3 introduces Canonical Space Supervision (CSS) that trains Gaussians to be object-aligned and amodally complete without per-image Gaussian labels. Sec. 4.4 summarizes architectural and training details. Our full pipeline is given in Fig. 2.

4.2. Assembling objects from dense predictions

Instance discovery. At inference time, for each pixel, we first compute the cosine similarity between the predicted embedding $\hat{\mathbf{e}}_{u,v}$ and a set of predefined category

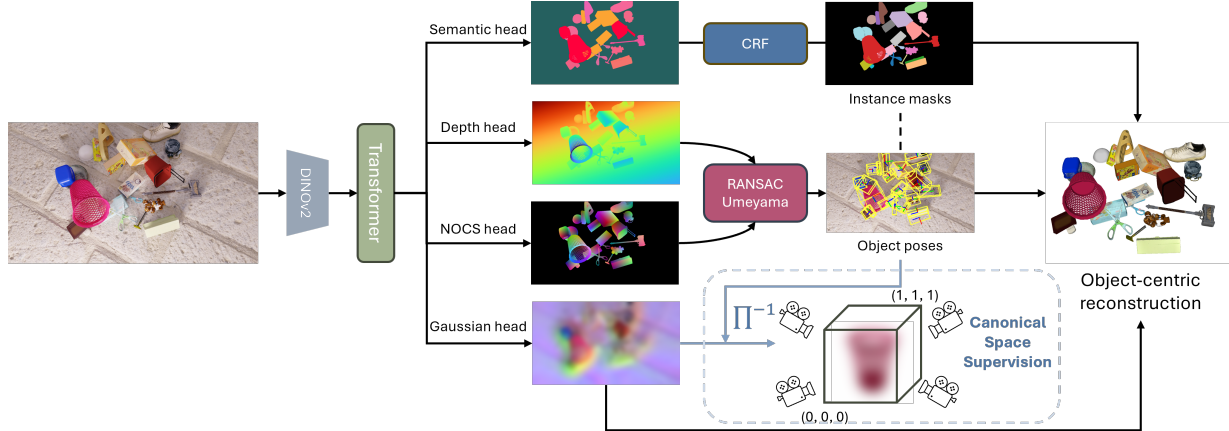


Figure 2. **Overview of our single-view object-centric 3D reconstruction pipeline.** Given a single RGB input, we extract dense DINOv2 features and feed them to a transformer that predicts per-pixel depth, CLIP-space semantic embeddings, NOCS coordinates, and Gaussian primitives. A CRF refines semantic affinities to produce coherent instance masks. For each instance, we estimate a category-level SIM(3) pose via RANSAC-Umeyama using the predicted NOCS-to-3D correspondences, enabling a transformation from camera space into the canonical object frame. The per-pixel Gaussians are then grouped and transformed into canonical space, where Canonical-Space Supervision (CSS) trains them to form amodally complete, compact 3D Gaussians. Aggregating all reconstructed objects yields an interactive, object-aligned scene representation from a single image.

name CLIP embeddings $\{l_c\}$. We then apply a fully connected conditional random field (CRF) [31], using unary potentials defined as $-\log \frac{\exp(\cos(\hat{e}_{u,v}, l_c)/\tau)}{\sum_{c'} \exp(\cos(\hat{e}_{u,v}, l_{c'})/\tau)}$ for each category c , where τ denotes the temperature parameter in the softmax function. Pairwise potentials are defined as $\cos(\hat{e}_{u,v}, \hat{e}_{u',v'})$. For more details about CRF, we refer the reader to [31]. This process yields groups $\{\hat{\mathcal{P}}_j\}$, where each $\hat{\mathcal{P}}_j$ represents the set of pixels corresponding to object j .

Pose estimation. With the pixels for each object instance identified, we use their predicted NOCS [62] coordinates $\mathbf{c}_{u,v}$ to determine the object’s precise SIM(3) pose in the scene. The NOCS coordinates establish a correspondence between a point’s observed position in the scene and its standardized position within a unit canonical cube. We can therefore solve for the similarity transformation $\hat{\Pi}_j = (\hat{s}_j, \hat{R}_j, \hat{\mathbf{t}}_j)$, representing the scale, rotation, and translation, which maps the canonical space of object j to the camera space. This is achieved by minimizing the alignment error between the back-projected 3D points and the transformed NOCS coordinates over all pixels belonging to that instance:

$$\hat{\Pi}_j = \arg \min_{\Pi} \sum_{(u,v) \in \hat{\mathcal{P}}_j} \|\hat{\mathbf{p}}_{u,v} - \Pi(\hat{\mathbf{c}}_{u,v})\|^2, \quad (3)$$

where $\Pi(\hat{\mathbf{c}}_{u,v}) = sR \cdot \hat{\mathbf{c}}_{u,v} + \mathbf{t}$. This optimization can be solved using Umeyama algorithm [61] with RANSAC [15]. The resulting inverse transformation, $\hat{\Pi}_j^{-1}$, gives us a direct mapping from the cluttered scene into the clean canonical space for each object. Notably, this NOCS prediction can also be used to differentiate object instances with the same category name but that are adjacent in the mask, where

CRF alone may not be enough. We run multiple RANSACs within each CRF-generated mask, and output objects when there are still enough inliers.

Object Gaussians. With the instance mask and estimated pose in hand, we obtain each object’s canonical-space Gaussian representation by transforming every predicted Gaussian mean as $\mu_{u,v}^{\text{can},(i)} = \hat{\Pi}_j^{-1}(\mu_{u,v}^{(i)})$ for all $(u,v) \in \hat{\mathcal{P}}_j, i \in \{1, \dots, k\}$. The resulting set of transformed Gaussians forms the complete canonical representation of object j .

Efficiency. Since OCH3R predicts all per-pixel quantities in one forward pass, every object is reconstructed at once. Our CUDA CRF runs in roughly 200 ms per image, and our CUDA RANSAC Umeyama adds under 10 ms per object, making its cost negligible. Consequently, runtime is nearly invariant to scene complexity and remains far below prior pipelines [56, 73, 83], which synthesize each object through iterative diffusion denoising and often require relation-graph optimization that grows quadratically with the number of objects.

4.3. Canonical-Space Supervision

One key challenge for our Gaussian prediction network is that it must infer a full, amodal set of object Gaussians from only the pixels that are actually visible. A natural idea is to use pre-optimized object Gaussians and place them in the camera frame so they can serve as ground-truth supervision. However, there lacks one-to-one correspondence between visible pixels and ground-truth object Gaussians. To address this, we introduce *Canonical Space Supervision* (Fig. 3), a strategy that transfers training signals to the ob-

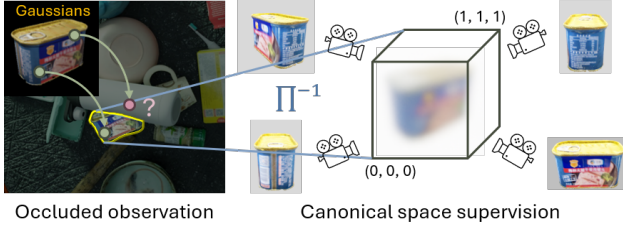


Figure 3. **Canonical Space Supervision (CSS)**. Predicted per-pixel Gaussians are transformed into the object’s canonical frame via the ground-truth pose Π^{-1} . In canonical space, they are supervised against pre-rendered multi-view ground-truth images, providing clean amodal signals that resolve occlusions and enforce compact, object-aligned Gaussian reconstructions.

ject’s canonical frame, where clean targets are available.

Concretely, we place each training object mesh in the canonical frame, and pre-render a set of N views $\mathcal{V} = \{I_n^{\text{gt}}\}_{n=1}^N$, where $I_n^{\text{gt}} \in \mathbb{R}^{H_{\text{can}} \times W_{\text{can}} \times 3}$. We set $N = 42$, $H_{\text{can}} = W_{\text{can}} = 512$. This is done once per object and reused across all images containing that object.

During training, we use ground truth object masks $\{\mathcal{P}_j\}$ to extract pixels of each object j . We transform the predicted Gaussians per object from the camera space into the canonical space with the ground truth object pose.

With the transformed Gaussians $\{g_{u,v}^{\text{can},(i)}\}$ of the object, we can render images of that object in its canonical space using the same camera angles as \mathcal{V} with a differentiable Gaussian rasterizer [29]. Let $\{\hat{I}_n\}_{n=1}^N$ denote the rendered images. Then the CSS loss is calculated by

$$\mathcal{L}_{\text{CSS}} = \sum_{n=1}^N \left(\|I_n^{\text{gt}} - \hat{I}_n\|_1 + \lambda_{\text{SSIM}}(1 - \text{SSIM}(I_n^{\text{gt}}, \hat{I}_n)) \right). \quad (4)$$

Occlusion handling via off-ray offsets. Each Gaussian mean is anchored at $\hat{\mathbf{p}}_{u,v}$ with a predicted camera-space offset $\Delta_{u,v}^{(i)}$, allowing a visible pixel to spawn Gaussians behind the first surface. Because CSS supervises in canonical space, occluded Gaussians receive gradients even when not visible in the input. Optionally, we regularize with an annealed small-offset prior: $\mathcal{L}_{\text{reg}} = \sum_{(u,v) \in \mathcal{P}_j} \sum_{i=1}^k \text{ReLU}(\|\Delta_{u,v}^{(i)} - \tau_{\text{offset}}\|_1)$.

4.4. Architecture and training details

Architecture. Inspired by VGGT [64], OCH3R uses a DINOv2 backbone [42] followed by a 48-layer ViT encoder and DPT-style decoder heads [46]. The input image is patchified by DINOv2 and processed by global self-attention through the encoder.

For dense tasks, each head takes features from four intermediate encoder layers (lateral skips), projects them to a common width, and upsamples to the image resolution with convolutional fusion.

For camera FOV prediction, we append a learnable camera token that is updated by a small stack of transformer blocks with adaptive layer-norm modulation and iterative refinement; a linear layer regresses the field-of-view angles $(\hat{\theta}_w, \hat{\theta}_h)$.¹

For Gaussian prediction we decouple geometry and appearance. A geometry head outputs per-pixel off-ray offsets $\Delta_{u,v}^{(i)}$ (for $i=1, \dots, k$), which are added to the back-projected point $\hat{\mathbf{p}}_{u,v}$ to obtain camera-frame means $\mu_{u,v}^{(i)}$. An appearance/shape head predicts canonical-frame scales $\sigma_{u,v}^{(i)}$, unit quaternions $\mathbf{q}_{u,v}^{\text{can},(i)}$, opacities $\alpha_{u,v}^{(i)}$, and SH coefficients $\mathbf{S}_{u,v}^{(i)}$. Following NoPoSplat [74], we provide an *RGB shortcut* to the appearance/shape head to improve fine texture details in 3D reconstruction. All parameters of each Gaussian and the k Gaussians of every pixel are simply concatenated.

Training. We optimize all tasks jointly with AdamW and a cosine learning-rate schedule. DINOv2 is initialized from public weights and fine-tuned end-to-end; the full list of hyperparameters is provided in the appendix.

Depth. We supervise canonical inverse depth as in Depth Pro [3]. Let f_w be the horizontal focal length (pixels) and W the image width, define $C = \frac{f_w}{W \cdot d}$. Our model outputs \hat{C} and is trained to minimize $\mathcal{L}_{\text{depth}} = \|\hat{C} - C\|_2 + \lambda \nabla \left(\|\nabla_x(\hat{C} - C)\|_2 + \|\nabla_y(\hat{C} - C)\|_2 \right)$. At test time, we recover metric depth by $\hat{d}_{u,v} := \frac{f_{\text{px}}}{W \cdot \hat{C}_{u,v}}$.

Semantics. During training time, we dynamically compute cosine similarities between the embedding of pixel and all the words that appear in the training image. We then encourage the embedding of the pixel to align with the ground-truth class by using the computed cosine similarities as the logits for softmax, with cross entropy loss.

NOCS. We reformulate NOCS coordinate regression as a bin classification task augmented with a learnable offset, which implicitly resolves ambiguities in symmetric objects. Each axis in NOCS (i.e., xyz) is discretized into $M=64$ centered bins. We supervise the bin classification using a cross-entropy loss and the offset prediction using a mean squared error loss. The total loss is averaged over all foreground object pixels.

Gaussians (CSS). Gaussian supervision follows Canonical Space Supervision discussed in Sec. 4.3.

Camera FOV. We supervise $(\hat{\theta}_w, \hat{\theta}_h)$ with a robust Huber loss on angles: $\mathcal{L}_{\text{cam}} = \|\hat{\theta}_w - \theta_w\|_{\epsilon} + \|\hat{\theta}_h - \theta_h\|_{\epsilon}$.

Task losses are combined with homoscedastic uncertainty weighting [28]; ablations are in the appendix.

¹Our implementation retains VGGT’s iterative refinement; translation/rotation channels are present in the token state but only FOV is used at test time.

5. Dataset

Existing indoor benchmarks for monocular depth estimation and open vocabulary semantic segmentation [10, 50, 51] primarily emphasize room layout and large furniture, while providing limited coverage of the object interaction scale that is central to everyday visual tasks. In contrast, progress in embodied perception [4, 14, 49, 66] and in mobile AR or MR systems [13, 20] requires accurate modeling of small, manipulable, and semantically diverse objects such as cups, tools, and containers that humans routinely interact with.

To support this direction, we construct a new evaluation benchmark by integrating several real world datasets tailored to this domain. Specifically, we include the validation split of HOPE [60] and the test splits of YCB Video [67], PACE [75], Omni6DPose [81] (OMNI), and NOCS [63]. For training, we curate and align four large scale sources: the training splits of PACE and Omni6DPose, Google Scanned Objects [12] renderings from Foundation-Pose [66], and HyperSim [48].

6. Experiments

We first evaluate holistic 3D object-centric reconstruction from a single RGB image in Sec. 6.1. Sec. 6.2 then demonstrates that beyond 3D reconstruction, our method also delivers state-of-the-art zero-shot performance on depth estimation, segmentation, and object pose prediction. Sec. 6.3 examines key design choices through targeted ablations.

6.1. 3D Reconstruction

We evaluate OCH3R against Gen3DSR [1], ACDC [11], and a unified glued baseline that uses instance masks from SAM2 [47] and GroundingDINO [39], object poses from MonoDiff9D [38], and depth from DepthPro [3]. We denote this pipeline as AoE (Army of Experts). Since the baselines are extremely slow, we randomly sample ten images from each dataset in our benchmark.

Following prior work [1, 73], we report Chamfer Distance and F-1@0.1 between the predicted and ground truth meshes, and CLIP similarity between the rendered and ground truth images. All backgrounds are manually normalized to white for both predictions and ground truth.

As shown in Tab. 1, our method establishes a clear margin over all baselines. On PACE, OCH3R reduces the Chamfer Distance from 0.31 (Gen3DSR) and 0.35 (AoE) to 0.18, while more than doubling the best F-1 score (45.00 versus AoE’s 21.39). Similar trends hold across all remaining datasets: on YCB-V, OCH3R achieves 0.17 CD (a 26 percent improvement over AoE and a 48 percent improvement over Gen3DSR) and reaches 22.71 F-1, surpassing the strongest baseline by over 10 points. On HOPE, OCH3R attains 83.69 CLIP similarity, exceeding Gen3DSR by +6.1

and AoE by +19.9. For NOCS real, OCH3R’s gains are the most pronounced, improving CD from 0.15 to 0.07 and F-1 from 38.01 to 76.77. These accuracy improvements come alongside a dramatic speedup: our 0.7 s inference time per image is roughly 2,000x faster than Gen3DSR (25.6 min) and ACDC (22.1 min), while also running more than 30x faster than AoE (21.6 s). It demonstrates the advantage of our unified per pixel prediction formulation. Some qualitative results are shown in Fig. 4.

6.2. Individual task performance

Zero-shot metric depth. Accurate metric depth from a single RGB image is essential to our pipeline, as it defines the anchor positions for our 3D Gaussians. We evaluate OCH3R on five datasets against seven state-of-the-art baselines using three standard metrics: δ_1 [33], AbsRel, and RMSE. Additional metrics (δ_2 , δ_3 , log10, RMSE_{log}, SI-log) are provided in the Supplementary.

As shown in Tab. 2, OCH3R achieves leading performance on all three metrics for PACE, HOPE, and NOCS-real, and on δ_1 for YCB-V. Although Metric3D V2 [22] and Depth Pro [3] perform slightly better on OMNI, the margin is minimal; moreover, Metric3D V2 requires ground-truth camera intrinsics, giving it an inherent advantage, yet it is still surpassed by OCH3R on four of the five datasets. Depth Anything V2 [72], trained primarily for relative depth and fine-tuned for metric estimation, shows high domain sensitivity, excelling on YCB-V (narrowly ahead of OCH3R) but degrading substantially elsewhere. Overall, OCH3R attains the best results in 10 of 15 metric-dataset combinations and delivers the strongest average performance across benchmarks.

Zero-shot semantic segmentation. Open-vocabulary semantic segmentation assigns per-pixel labels drawn from a potentially open set of natural-language concepts. To build an evaluation vocabulary disjoint from training, we aggregate names from the test datasets, common indoor categories from ADE20K [84, 85], and additional household items.

We report standard OVSS metrics: mIoU and FB-IoU. Given the difficulty of segmenting fine-grained, cluttered indoor scenes, we additionally report hit@5, which allows each method to produce up to five candidate labels per pixel. Since FB-IoU already captures the ability to separate foreground from background, the remaining metrics are computed on foreground regions only.

Tab. 3 compares OCH3R with seven OVSS baselines. Across five datasets and three metrics (15 settings), OCH3R ranks first in 12 and achieves the best average rank (1.27). It leads all three metrics on PACE, YCB-V, and NOCS-Real; mIoU and FB-IoU on HOPE; and FB-IoU on OMNI. Averaged across datasets, OCH3R obtains 11.04 mIoU, 83.18 FB-IoU, and 83.56 hit@5, outperforming the strongest

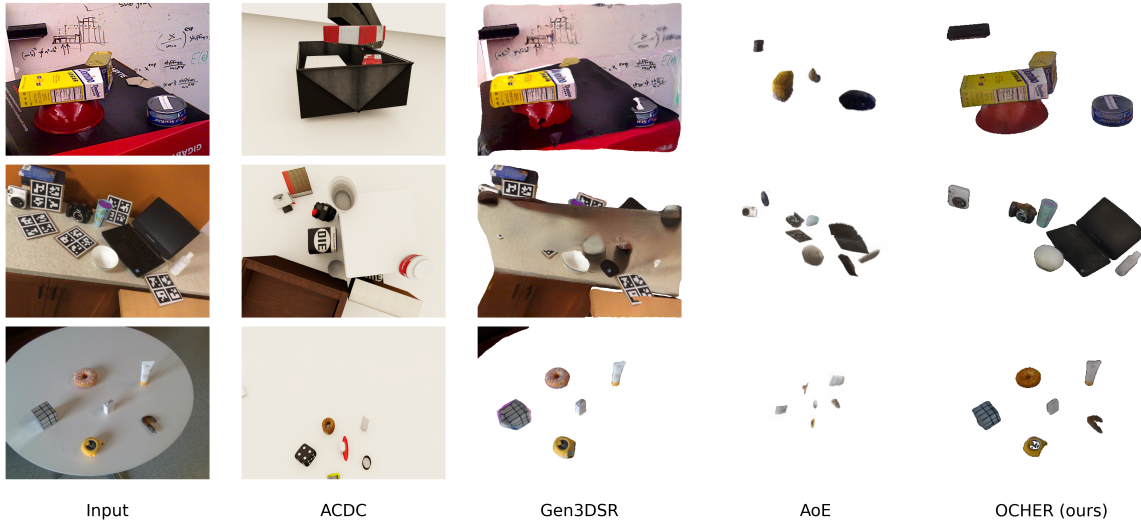


Figure 4. **Qualitative comparison of single-image 3D object-centric reconstruction.** Given a single RGB input, we compare our method (OCH3R) with ACDC, Gen3DSR, and AoE (Army of Experts: SAM2 + GroundingDINO + MonoDiff9D + DepthPro). Prior methods often yield incomplete geometry, distorted textures, or missing objects. OCH3R reconstructs sharper, more complete, and semantically consistent objects across diverse scenes.

Model	PACE			OMNI			YCB-V			HOPE			NOCS real			Time per image↓
	CD↓	F-1↑	CLIP↑	CD↓	F-1↑	CLIP↑	CD↓	F-1↑	CLIP↑	CD↓	F-1↑	CLIP↑	CD↓	F-1↑	CLIP↑	
ACDC [11]	0.69	0.00	73.74	-	-	72.23	0.32	7.76	60.15	1.42	1.92	63.75	3.44	1.72	69.74	22.1 min
Gen3DSR [1]	<u>0.31</u>	12.93	<u>81.61</u>	-	-	<u>82.00</u>	0.33	8.85	<u>75.26</u>	0.35	12.05	<u>77.63</u>	0.26	17.73	<u>75.33</u>	25.6 min
AoE	0.35	<u>21.39</u>	77.97	-	-	69.31	<u>0.23</u>	<u>12.45</u>	66.05	<u>0.18</u>	47.71	63.80	<u>0.15</u>	<u>38.01</u>	70.62	21.6 s
OCH3R (ours)	0.18	45.00	83.15	-	-	82.78	0.17	22.71	78.80	0.14	<u>40.08</u>	83.69	0.07	76.77	85.90	0.7 s

Table 1. Comparison of 3D reconstruction and semantic consistency across datasets using CD (Chamfer Distance, lower is better), F-1 score, and CLIP similarity.

baseline by +2.44 mIoU (MAFT+ [27]), +36.80 FB-IoU (SAN [70]), and +2.47 hit@5 (MAFT+).

Zero-shot pose estimation. We further evaluate OCH3R’s ability to recover category-level 6D object poses from a single RGB image in a zero-shot setting. Due to space constraints, the full quantitative comparison with AG-Pose [37], SecondPose [7], and MonoDiff9D [38] across five indoor benchmarks is provided in the Supplementary. AG-Pose and SecondPose require RGB-D inputs, so we supply them with our predicted depths. Following MonoDiff9D, we report accuracy within 10 cm, within 10°, and under the joint 10°/10 cm criterion.

Across all datasets, OCH3R shows consistent gains on the stricter angular and joint metrics. It attains the highest 10° and joint accuracy on PACE and HOPE and improves the joint metric on NOCS-real. For example, on PACE, OCH3R improves the 10° rate from 15.1 to 25.9 and the joint 10°/10 cm rate from 8.6 to 14.0 compared to AG-Pose. These results indicate that the unified 3D representation learned by OCH3R naturally supports precise, canonically aligned object poses without any dataset-specific fine-tuning.

In summary, our model’s strong performance across monocular depth estimation, open-vocabulary semantic segmentation, and pose estimation jointly enables state-of-the-art 3D reconstruction quality, producing geometrically precise, semantically coherent, and canonically aligned scene representations.

6.3. Ablation

Multi-task learning. To demonstrate the advantage of using a unified model for multiple traditionally separated tasks, we retrain the model while removing one head at a time. Experiments shows that dropping semantic embeddings causes large pose and Gaussian degradations and also hurts depth. More broadly, removing any head weakens the remaining tasks, and the full four-head variant performs best. Full per-dataset quantitative results are provided in the Supplementary.

Offset in camera space vs. directly in canonical space.

We also tried predicting Gaussian parameters directly in the canonical frame, bypassing the offset-along-ray formulation. As shown in Fig. 5, removing the geometric scaffold of camera rays causes the network to collapse into

Model	PACE			OMNI			YCB-V			HOPE			NOCS real		
	$\delta_1\uparrow$	AbsRel \downarrow	RMSE \downarrow	$\delta_1\uparrow$	AbsRel \downarrow	RMSE \downarrow	$\delta_1\uparrow$	AbsRel \downarrow	RMSE \downarrow	$\delta_1\uparrow$	AbsRel \downarrow	RMSE \downarrow	$\delta_1\uparrow$	AbsRel \downarrow	RMSE \downarrow
NeWCRFs [78]	17.00	0.7356	0.5308	21.41	0.6432	0.9934	52.71	0.2740	0.2699	5.37	0.8073	0.5029	36.00	0.3352	0.3586
ZoeDepth [2]	8.20	0.8508	0.6146	20.73	0.5794	0.9406	52.84	0.2704	0.2750	0.53	0.9814	0.6055	34.08	0.4399	0.5275
Metric3D V2 [22]	1.32	0.4695	0.3995	73.73	0.1788	<u>0.7963</u>	15.44	0.2791	0.2538	0.01	0.4039	0.2968	8.50	0.3273	0.3571
Depth Anything V2 [72]	13.07	0.7373	0.5906	5.83	0.9009	1.1728	50.74	<u>0.1899</u>	0.2029	0.07	1.0364	0.6518	2.44	0.5507	0.6088
Depth Pro [3]	33.63	0.5603	0.5610	<u>57.37</u>	0.2742	0.7940	49.04	0.2078	0.2148	23.09	<u>0.4035</u>	0.3013	81.58	0.1370	0.1831
VGGT [64]	<u>55.58</u>	<u>0.2415</u>	<u>0.2096</u>	57.14	<u>0.2272</u>	1.0365	63.88	0.1822	0.2131	<u>37.17</u>	0.4313	<u>0.2844</u>	<u>92.26</u>	<u>0.0965</u>	<u>0.1394</u>
UniDepth V2 [43]	35.05	0.5076	0.4820	22.80	0.7221	1.1007	32.70	0.2548	0.2499	8.63	0.7622	0.6830	78.92	0.1778	0.2366
OCH3R (ours)	94.82	0.0834	0.1039	42.77	0.2900	0.8042	69.96	0.1933	<u>0.2044</u>	61.36	0.2192	0.1812	98.43	0.0923	0.1066

Table 2. **Monocular metric depth estimation results** on PACE, OMNI, YCB-V, HOPE, and NOCS real. Each dataset block reports δ_1 (in percentage), AbsRel, and RMSE. Bold indicates the best result, and underline indicates the second best.

Model	PACE			OMNI			YCB-V			HOPE			NOCS real		
	mIoU \uparrow	FB-IoU \uparrow	hit@5 \uparrow	mIoU \uparrow	FB-IoU \uparrow	hit@5 \uparrow	mIoU \uparrow	FB-IoU \uparrow	hit@5 \uparrow	mIoU \uparrow	FB-IoU \uparrow	hit@5 \uparrow	mIoU \uparrow	FB-IoU \uparrow	hit@5 \uparrow
LSeg [34]	0.26	17.23	8.52	2.43	4.55	16.31	2.63	12.41	23.05	0.30	12.09	20.69	5.48	8.73	79.82
OVSeg [36]	1.28	13.57	28.84	11.24	2.94	52.19	1.29	12.20	58.66	0.31	11.87	25.99	1.87	8.54	79.21
ODISE [69]	1.69	13.70	36.05	13.27	3.66	58.54	4.51	12.17	76.76	0.99	11.87	68.77	6.31	8.53	90.60
FC-CLIP [77]	<u>3.67</u>	13.56	61.62	<u>22.29</u>	3.61	71.11	3.69	12.15	69.96	1.85	11.91	71.80	4.72	9.40	94.68
CAT-Seg [9]	1.26	21.48	30.53	9.61	4.14	52.62	2.38	12.12	65.78	2.87	11.91	75.97	5.31	8.79	95.80
SAN [70]	1.70	<u>71.05</u>	31.87	13.75	<u>40.82</u>	53.09	4.25	<u>44.77</u>	72.83	<u>3.27</u>	<u>29.96</u>	63.94	5.22	<u>45.30</u>	94.56
MAFT+ [27]	3.66	13.76	<u>64.39</u>	23.02	3.61	76.69	<u>5.00</u>	12.16	<u>79.01</u>	3.21	11.87	89.23	<u>8.10</u>	8.53	<u>96.14</u>
OCH3R (ours)	7.34	94.95	84.76	18.43	84.21	<u>75.23</u>	9.14	72.00	80.03	6.90	71.78	<u>79.27</u>	13.40	92.95	98.51

Table 3. **Open-vocabulary semantic segmentation results** on PACE, OMNI, YCB-V, HOPE, and NOCS real. Each dataset block reports mIoU, FB-IoU, and hit@5 in percentages. Bold indicates the best result, and underline indicates the second best.

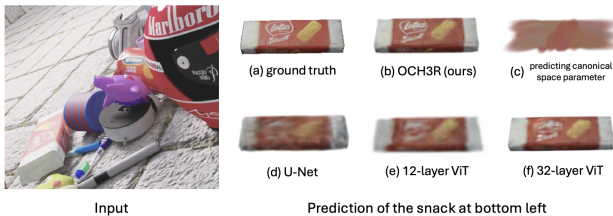


Figure 5. Qualitative ablations showing that (i) predicting Gaussians directly in canonical space collapses, and (ii) OCH3R’s formulation remains robust across model scales and architectures.

an unstructured blob, confirming that unconstrained pixel-to-Gaussian mapping is highly underdetermined. By instead predicting per-pixel offsets in camera space and using Canonical-Space Supervision to organize the final layout, OCH3R obtains a stable and expressive inductive bias that enables high-quality reconstruction.

Model scale and architecture. The core of our method, particularly the multi-task learning paradigm and Canonical-Space Supervision, is orthogonal to model architecture, so in principle any dense predictor could be used. We validate this by testing a U-Net (matched in parameter count to the 32-layer ViT) and two smaller ViT variants. As shown in Fig. 5, while larger models yield sharper textures and cleaner geometry, all architectures successfully recover the object’s overall shape. This confirms that OCH3R’s pipeline transfers across dense predictors and scales well with model capacity.

7. Conclusion

In this paper, we try to address the long standing problem of understanding a scene as a set of discrete, posed objects from a single RGB image. Rather than relying on multi stage pipelines that decompose the task into segmentation, per object reconstruction, and post hoc alignment, we proposed OCH3R, a unified, feed forward model that predicts all object instances, their category level SIM(3) poses, and high fidelity 3D Gaussians in a single pass. The key ingredients are a transformer that produces dense, pixel aligned attributes (metric depth, CLIP based semantics, NOCS coordinates, and per pixel Gaussians), a simple inference procedure for instance discovery and pose estimation, and canonical space supervision that trains amodally complete Gaussians without per image Gaussian labels.

To support this setting, we assembled a large scale dataset for holistic object centric 3D scene representation by aligning PACE, Omni6DPose, HOPE, YCB-Video and NOCS into a unified benchmark with per instance masks, semantics, 6D poses, and 3D models. Across this benchmark, OCH3R outperforms previous baselines on monocular depth estimation, open vocabulary segmentation, and category level pose prediction, while producing more complete, editable 3D object reconstructions with feed forward inference that scales essentially independently of the number of objects.

References

- [1] Andreea Ardelean, Mert Özer, and Bernhard Egger. Generalizable 3d scene reconstruction via divide and conquer from a single view. In *International Conference on 3D Vision (3DV)*, pages 616–626, 2025. 3, 6, 7
- [2] Shariq Farooq Bhat, Reiner Birkel, Diana Wofk, Peter Wonka, and Matthias Müller. Zoedepth: Zero-shot transfer by combining relative and metric depth, 2023. 8
- [3] Aleksei Bochkovskii, Amaël Delaunoy, Hugo Germain, Marcel Santos, Yichao Zhou, Stephan R. Richter, and Vladlen Koltun. Depth pro: Sharp monocular metric depth in less than a second, 2025. 5, 6, 8
- [4] Anthony Brohan, Noah Brown, Justice Carbajal, Yevgen Chebotar, Xi Chen, Krzysztof Choromanski, Tianli Ding, Danny Driess, Avinava Dubey, Chelsea Finn, Pete Florence, Chuyuan Fu, Montse Gonzalez Arenas, Keerthana Gopalakrishnan, Kehang Han, Karol Hausman, Alexander Herzog, Jasmine Hsu, Brian Ichter, Alex Irpan, Nikhil Joshi, Ryan Julian, Dmitry Kalashnikov, Yuheng Kuang, Isabel Leal, Lisa Lee, Tsang-Wei Edward Lee, Sergey Levine, Yao Lu, Henryk Michalewski, Igor Mordatch, Karl Pertsch, Kanishk Rao, Krista Reymann, Michael Ryoo, Grecia Salazar, Pannag Sanketi, Pierre Sermanet, Jaspier Singh, Anikait Singh, Radu Soricut, Huong Tran, Vincent Vanhoucke, Quan Vuong, Ayzaan Wahid, Stefan Welker, Paul Wohlhart, Jialin Wu, Fei Xia, Ted Xiao, Peng Xu, Sichun Xu, Tianhe Yu, and Brianna Zitkovich. Rt-2: Vision-language-action models transfer web knowledge to robotic control, 2023. 6
- [5] David Charatan, Sizhe Li, Andrea Tagliasacchi, and Vincent Sitzmann. pixelsplat: 3d gaussian splats from image pairs for scalable generalizable 3d reconstruction, 2024. 2, 3
- [6] Anpei Chen, Haofei Xu, Stefano Esposito, Siyu Tang, and Andreas Geiger. Lara: Efficient large-baseline radiance fields, 2024. 3
- [7] Yamei Chen, Yan Di, Guangyao Zhai, Fabian Manhardt, Chenyangguang Zhang, Ruida Zhang, Federico Tombari, Nassir Navab, and Benjamin Busam. Secondpose: Se(3)-consistent dual-stream feature fusion for category-level pose estimation. In *Proceedings of the IEEE/CVF Conference on Computer Vision and Pattern Recognition (CVPR)*, pages 9959–9969, 2024. 7
- [8] Yuedong Chen, Haofei Xu, Chuanxia Zheng, Bohan Zhuang, Marc Pollefeys, Andreas Geiger, Tat-Jen Cham, and Jianfei Cai. *MVSplat: Efficient 3D Gaussian Splatting from Sparse Multi-view Images*, page 370–386. Springer Nature Switzerland, 2024. 2, 3
- [9] Seokju Cho, Heeseong Shin, Sunghwan Hong, Anurag Arnab, Paul Hongsuck Seo, and Seungryong Kim. Cat-seg: Cost aggregation for open-vocabulary semantic segmentation, 2024. 8
- [10] Angela Dai, Angel X. Chang, Manolis Savva, Maciej Halber, Thomas Funkhouser, and Matthias Nießner. Scannet: Richly-annotated 3d reconstructions of indoor scenes, 2017. 6
- [11] Tianyuan Dai, Josiah Wong, Yunfan Jiang, Chen Wang, Cem Gokmen, Ruohan Zhang, Jiajun Wu, and Li Fei-Fei. Automated creation of digital cousins for robust policy learning. In *Conference on Robot Learning (CoRL)*, 2024. 6, 7
- [12] Laura Downs, Anthony Francis, Nate Koenig, Brandon Kinman, Ryan Hickman, Krista Reymann, Thomas B. McHugh, and Vincent Vanhoucke. Google scanned objects: A high-quality dataset of 3d scanned household items, 2022. 2, 6
- [13] Ruofei Du, Eric Turner, Maksym Dzitsiuk, Luca Prasso, Ivo Duarte, Jason Dourgarian, Joao Afonso, Jose Pascoal, Josh Gladstone, Nuno Cruces, Shahram Izadi, Adarsh Kowdle, Konstantine Tsotsos, and David Kim. Depthlab: Real-time 3d interaction with depth maps for mobile augmented reality. In *Proceedings of the 33rd Annual ACM Symposium on User Interface Software and Technology*, page 829–843, New York, NY, USA, 2020. Association for Computing Machinery. 6
- [14] Hao-Shu Fang, Chenxi Wang, Minghao Gou, and Cewu Lu. Graspnet-1billion: A large-scale benchmark for general object grasping. In *Proceedings of the IEEE/CVF Conference on Computer Vision and Pattern Recognition (CVPR)*, 2020. 6
- [15] Martin A. Fischler and Robert C. Bolles. Random sample consensus: a paradigm for model fitting with applications to image analysis and automated cartography. *Commun. ACM*, 24(6):381–395, 1981. 4
- [16] Yiming Gao, Yan-Pei Cao, and Ying Shan. Surfelfnerf: Neural surfel radiance fields for online photorealistic reconstruction of indoor scenes, 2023. 2
- [17] Georgia Gkioxari, Jitendra Malik, and Justin Johnson. Mesh r-cnn, 2020. 2
- [18] Thibault Groueix, Matthew Fisher, Vladimir G. Kim, Bryan C. Russell, and Mathieu Aubry. Atlasnet: A papier-mâché approach to learning 3d surface generation, 2018. 2
- [19] Can Gümeli, Angela Dai, and Matthias Nießner. Roca: Robust cad model retrieval and alignment from a single image. In *Proceedings of the IEEE/CVF Conference on Computer Vision and Pattern Recognition (CVPR)*, pages 4022–4031, 2022. 3
- [20] Aleksander Holynski and Johannes Kopf. Fast depth densification for occlusion-aware augmented reality. *ACM Transactions on Graphics (TOG)*, 37(6), 2018. 6
- [21] Yicong Hong, Kai Zhang, Jiuxiang Gu, Sai Bi, Yang Zhou, Difan Liu, Feng Liu, Kalyan Sunkavalli, Trung Bui, and Hao Tan. Lrm: Large reconstruction model for single image to 3d, 2024. 2
- [22] Mu Hu, Wei Yin, Chi Zhang, Zhipeng Cai, Xiaoxiao Long, Hao Chen, Kaixuan Wang, Gang Yu, Chunhua Shen, and Shaojie Shen. Metric3d v2: A versatile monocular geometric foundation model for zero-shot metric depth and surface normal estimation. *IEEE Transactions on Pattern Analysis and Machine Intelligence*, 46(12):10579–10596, 2024. 6, 8
- [23] Zehuan Huang, Yuan-Chen Guo, Xingqiao An, Yunhan Yang, Yangguang Li, Zi-Xin Zou, Ding Liang, Xihui Liu, Yan-Pei Cao, and Lu Sheng. Midi: Multi-instance diffusion for single image to 3d scene generation, 2025. 3
- [24] Muhammad Zubair Irshad, Thomas Kollar, Michael Laskey, Kevin Stone, and Zsolt Kira. Centersnap: Single-shot multi-object 3d shape reconstruction and categorical 6d pose and size estimation, 2022. 2, 3

- [25] Muhammad Zubair Irshad, Sergey Zakharov, Rares Ambrus, Thomas Kollar, Zsolt Kira, and Adrien Gaidon. Shapo: Implicit representations for multi-object shape, appearance, and pose optimization, 2022. 2, 3
- [26] Hamid Izadinia, Qi Shan, and Steven M. Seitz. Im2cad, 2017. 2
- [27] Siyu Jiao, Hongguang Zhu, Jiannan Huang, Yao Zhao, Yunchao Wei, and Humphrey Shi. Collaborative vision-text representation optimizing for open-vocabulary segmentation, 2024. 7, 8
- [28] Alex Kendall, Yarin Gal, and Roberto Cipolla. Multi-task learning using uncertainty to weigh losses for scene geometry and semantics, 2018. 5
- [29] Bernhard Kerbl, Georgios Kopanas, Thomas Leimkühler, and George Drettakis. 3d gaussian splatting for real-time radiance field rendering. *ACM Trans. Graph.*, 42(4):139–1, 2023. 2, 5
- [30] Bernhard Kerbl, Georgios Kopanas, Thomas Leimkühler, and George Drettakis. 3d gaussian splatting for real-time radiance field rendering, 2023. 2, 3
- [31] Philipp Krähenbühl and Vladlen Koltun. Efficient inference in fully connected crfs with gaussian edge potentials. *Advances in neural information processing systems*, 24, 2011. 4
- [32] Weicheng Kuo, Anelia Angelova, Tsung-Yi Lin, and Angela Dai. Mask2cad: 3d shape prediction by learning to segment and retrieve, 2020. 3
- [33] Lubor Ladicky, Jianbo Shi, and Marc Pollefeys. Pulling things out of perspective. In *Proceedings of the IEEE Conference on Computer Vision and Pattern Recognition (CVPR)*, 2014. 6
- [34] Boyi Li, Kilian Q. Weinberger, Serge Belongie, Vladlen Koltun, and René Ranftl. Language-driven semantic segmentation, 2022. 3, 8
- [35] Jiaxin Li, Zijian Feng, Qi She, Henghui Ding, Changhu Wang, and Gim Hee Lee. Mine: Towards continuous depth mpi with nerf for novel view synthesis, 2021. 2
- [36] Feng Liang, Bichen Wu, Xiaoliang Dai, Kunpeng Li, Yinan Zhao, Hang Zhang, Peizhao Zhang, Peter Vajda, and Diana Marculescu. Open-vocabulary semantic segmentation with mask-adapted clip, 2023. 8
- [37] Xiao Lin, Wenfei Yang, Yuan Gao, and Tianzhu Zhang. Instance-adaptive and geometric-aware keypoint learning for category-level 6d object pose estimation. In *Proceedings of the IEEE/CVF Conference on Computer Vision and Pattern Recognition*, pages 21040–21049, 2024. 7
- [38] Jian Liu, Wei Sun, Hui Yang, Jin Zheng, Zichen Geng, Hossein Rahmani, and Ajmal Mian. Monodiff9d: Monocular category-level 9d object pose estimation via diffusion model. In *IEEE International Conference on Robotics and Automation (ICRA)*, 2025. 6, 7
- [39] Shilong Liu, Zhaoyang Zeng, Tianhe Ren, Feng Li, Hao Zhang, Jie Yang, Qing Jiang, Chunyuan Li, Jianwei Yang, Hang Su, et al. Grounding dino: Marrying dino with grounded pre-training for open-set object detection. In *European conference on computer vision*, pages 38–55. Springer, 2024. 6
- [40] Ben Mildenhall, Pratul P. Srinivasan, Matthew Tancik, Jonathan T. Barron, Ravi Ramamoorthi, and Ren Ng. Nerf: Representing scenes as neural radiance fields for view synthesis, 2020. 3
- [41] Yinyu Nie, Xiaoguang Han, Shihui Guo, Yujian Zheng, Jian Chang, and Jian Jun Zhang. Total3dunderstanding: Joint layout, object pose and mesh reconstruction for indoor scenes from a single image, 2020. 2
- [42] Maxime Oquab, Timothée Darcet, Théo Moutakanni, Huy Vo, Marc Szafraniec, Vasil Khalidov, Pierre Fernandez, Daniel Haziza, Francisco Massa, Alaaeldin El-Nouby, Mahmoud Assran, Nicolas Ballas, Wojciech Galuba, Russell Howes, Po-Yao Huang, Shang-Wen Li, Ishan Misra, Michael Rabbat, Vasu Sharma, Gabriel Synnaeve, Hu Xu, Hervé Jegou, Julien Mairal, Patrick Labatut, Armand Joulin, and Piotr Bojanowski. Dinov2: Learning robust visual features without supervision, 2024. 5
- [43] Luigi Piccinelli, Christos Sakaridis, Yung-Hsu Yang, Mattia Segu, Siyuan Li, Wim Abbeels, and Luc Van Gool. Unidepthv2: Universal monocular metric depth estimation made simpler, 2025. 8
- [44] Stefan Popov, Pablo Bauszat, and Vittorio Ferrari. Corenet: Coherent 3d scene reconstruction from a single rgb image, 2020. 2
- [45] Alec Radford, Jong Wook Kim, Chris Hallacy, Aditya Ramesh, Gabriel Goh, Sandhini Agarwal, Girish Sastry, Amanda Askell, Pamela Mishkin, Jack Clark, Gretchen Krueger, and Ilya Sutskever. Learning transferable visual models from natural language supervision, 2021. 2, 3
- [46] René Ranftl, Alexey Bochkovskiy, and Vladlen Koltun. Vision transformers for dense prediction, 2021. 5
- [47] Nikhila Ravi, Valentin Gabeur, Yuan-Ting Hu, Ronghang Hu, Chaitanya Ryali, Tengyu Ma, Haitham Khedr, Roman Rädle, Chloe Rolland, Laura Gustafson, et al. Sam 2: Segment anything in images and videos. *arXiv preprint arXiv:2408.00714*, 2024. 6
- [48] Mike Roberts, Jason Ramapuram, Anurag Ranjan, Atulit Kumar, Miguel Angel Bautista, Nathan Paczan, Russ Webb, and Joshua M. Susskind. Hypersim: A photorealistic synthetic dataset for holistic indoor scene understanding, 2021. 2, 6
- [49] Mohit Shridhar, Lucas Manuelli, and Dieter Fox. Perceiver-actor: A multi-task transformer for robotic manipulation, 2022. 6
- [50] Nathan Silberman, Derek Hoiem, Pushmeet Kohli, and Rob Fergus. Indoor segmentation and support inference from rgb-d images. In *Proceedings of the 12th European Conference on Computer Vision (ECCV)*, pages 746–760, Berlin, Heidelberg, 2012. Springer. 6
- [51] Shuran Song, Samuel P. Lichtenberg, and Jianxiong Xiao. Sun rgb-d: A rgb-d scene understanding benchmark suite. In *Proceedings of the IEEE Conference on Computer Vision and Pattern Recognition (CVPR)*, pages 567–576, 2015. 6
- [52] Stanislaw Szymanowicz, Christian Rupprecht, and Andrea Vedaldi. Splatter image: Ultra-fast single-view 3d reconstruction. In *Proceedings of the IEEE/CVF conference on computer vision and pattern recognition*, pages 10208–10217, 2024. 2, 3

- [53] Stanislaw Szymanowicz, Eldar Insafutdinov, Chuanxia Zheng, Dylan Campbell, Joao F Henriques, Christian Rupprecht, and Andrea Vedaldi. Flash3d: Feed-forward generalisable 3d scene reconstruction from a single image. In *2025 International Conference on 3D Vision (3DV)*, pages 670–681. IEEE, 2025. 2
- [54] Stanislaw Szymanowicz, Eldar Insafutdinov, Chuanxia Zheng, Dylan Campbell, João F. Henriques, Christian Rupprecht, and Andrea Vedaldi. Flash3d: Feed-forward generalisable 3d scene reconstruction from a single image, 2025. 2, 3
- [55] Jiaxiang Tang, Zhaoxi Chen, Xiaokang Chen, Tengfei Wang, Gang Zeng, and Ziwei Liu. Lgm: Large multi-view gaussian model for high-resolution 3d content creation, 2024. 2, 3
- [56] Jiapeng Tang, Yinyu Nie, Lev Markhasin, Angela Dai, Justus Thies, and Matthias Nießner. Diffuscene: Denoising diffusion models for generative indoor scene synthesis, 2024. 4
- [57] Maxim Tatarchenko, Alexey Dosovitskiy, and Thomas Brox. Octree generating networks: Efficient convolutional architectures for high-resolution 3d outputs, 2017. 2
- [58] Shubham Tulsiani, Tinghui Zhou, Alexei A. Efros, and Jitendra Malik. Multi-view supervision for single-view reconstruction via differentiable ray consistency, 2017. 2
- [59] Shubham Tulsiani, Richard Tucker, and Noah Snavely. Layer-structured 3d scene inference via view synthesis, 2018. 2
- [60] Stephen Tyree, Jonathan Tremblay, Thang To, Jia Cheng, Terry Mosier, Jeffrey Smith, and Stan Birchfield. 6-dof pose estimation of household objects for robotic manipulation: An accessible dataset and benchmark, 2022. 6
- [61] S. Umeyama. Least-squares estimation of transformation parameters between two point patterns. *IEEE Transactions on Pattern Analysis and Machine Intelligence*, 13(4):376–380, 1991. 4
- [62] He Wang, Srinath Sridhar, Jingwei Huang, Julien Valentin, Shuran Song, and Leonidas J Guibas. Normalized object coordinate space for category-level 6d object pose and size estimation. In *Proceedings of the IEEE/CVF conference on computer vision and pattern recognition*, pages 2642–2651, 2019. 2, 4
- [63] He Wang, Srinath Sridhar, Jingwei Huang, Julien Valentin, Shuran Song, and Leonidas J. Guibas. Normalized object coordinate space for category-level 6d object pose and size estimation, 2019. 3, 6
- [64] Jianyuan Wang, Minghao Chen, Nikita Karaev, Andrea Vedaldi, Christian Rupprecht, and David Novotny. Vggt: Visual geometry grounded transformer, 2025. 3, 5, 8
- [65] Yunsong Wang, Tianxin Huang, Hanlin Chen, and Gim Hee Lee. Freesplat: Generalizable 3d gaussian splatting towards free-view synthesis of indoor scenes, 2024. 2, 3
- [66] Bowen Wen, Wei Yang, Jan Kautz, and Stan Birchfield. Foundationpose: Unified 6d pose estimation and tracking of novel objects, 2024. 6
- [67] Yu Xiang, Tanner Schmidt, Venkatraman Narayanan, and Dieter Fox. Posecnn: A convolutional neural network for 6d object pose estimation in cluttered scenes. In *Proceedings of Robotics: Science and Systems (RSS)*, 2018. 6
- [68] Haofei Xu, Songyou Peng, Fangjinhua Wang, Hermann Blum, Daniel Barath, Andreas Geiger, and Marc Pollefeys. Depthsplat: Connecting gaussian splatting and depth, 2025. 2
- [69] Jiarui Xu, Sifei Liu, Arash Vahdat, Wonmin Byeon, Xiaolong Wang, and Shalini De Mello. Open-vocabulary panoptic segmentation with text-to-image diffusion models, 2023. 8
- [70] Mengde Xu, Zheng Zhang, Fangyun Wei, Han Hu, and Xiang Bai. Side adapter network for open-vocabulary semantic segmentation, 2023. 7, 8
- [71] Yinghao Xu, Zifan Shi, Wang Yifan, Hansheng Chen, Ceyuan Yang, Sida Peng, Yujun Shen, and Gordon Wetstein. Grm: Large gaussian reconstruction model for efficient 3d reconstruction and generation, 2024. 2, 3
- [72] Lihe Yang, Bingyi Kang, Zilong Huang, Zhen Zhao, Xiaogang Xu, Jiashi Feng, and Hengshuang Zhao. Depth anything v2, 2024. 6, 8
- [73] Kaixin Yao, Longwen Zhang, Xinhao Yan, Yan Zeng, Qixuan Zhang, Wei Yang, Lan Xu, Jiayuan Gu, and Jingyi Yu. Cast: Component-aligned 3d scene reconstruction from an rgb image, 2025. 2, 3, 4, 6
- [74] Botao Ye, Sifei Liu, Haofei Xu, Xueting Li, Marc Pollefeys, Ming-Hsuan Yang, and Songyou Peng. No pose, no problem: Surprisingly simple 3d gaussian splats from sparse unposed images, 2024. 2, 3, 5
- [75] Yang You, Kai Xiong, Zhening Yang, Zhengxiang Huang, Junwei Zhou, Ruoxi Shi, Zhou Fang, Adam W. Harley, Leonidas Guibas, and Cewu Lu. Pace: A large-scale dataset with pose annotations in cluttered environments, 2024. 2, 6
- [76] Alex Yu, Vickie Ye, Matthew Tancik, and Angjoo Kanazawa. pixelnerf: Neural radiance fields from one or few images, 2021. 2
- [77] Qihang Yu, Ju He, Xueqing Deng, Xiaohui Shen, and Liang-Chieh Chen. Convolutions die hard: Open-vocabulary segmentation with single frozen convolutional clip, 2023. 8
- [78] Weihao Yuan, Xiaodong Gu, Zuozhuo Dai, Siyu Zhu, and Ping Tan. New crfs: Neural window fully-connected crfs for monocular depth estimation, 2022. 8
- [79] Cheng Zhang, Zhaopeng Cui, Yinda Zhang, Bing Zeng, Marc Pollefeys, and Shuaicheng Liu. Holistic 3d scene understanding from a single image with implicit representation, 2021. 2
- [80] Chubin Zhang, Hongliang Song, Yi Wei, Yu Chen, Jiwen Lu, and Yansong Tang. Geolrm: Geometry-aware large reconstruction model for high-quality 3d gaussian generation, 2024. 2
- [81] Jiyao Zhang, Weiyao Huang, Bo Peng, Mingdong Wu, Fei Hu, Zijian Chen, Bo Zhao, and Hao Dong. Omni6dpose: A benchmark and model for universal 6d object pose estimation and tracking, 2024. 2, 6
- [82] Kai Zhang, Sai Bi, Hao Tan, Yuanbo Xiangli, Nanxuan Zhao, Kalyan Sunkavalli, and Zexiang Xu. Gs-lrm: Large reconstruction model for 3d gaussian splatting, 2024. 2, 3
- [83] Qingcheng Zhao, Xiang Zhang, Haiyang Xu, Zeyuan Chen, Jianwen Xie, Yuan Gao, and Zhuowen Tu. Depr: Depth guided single-view scene reconstruction with instance-level diffusion, 2025. 3, 4

- [84] Bolei Zhou, Hang Zhao, Xavier Puig, Sanja Fidler, Adela Barriuso, and Antonio Torralba. Scene parsing through ade20k dataset. In *Proceedings of the IEEE Conference on Computer Vision and Pattern Recognition*, 2017. [6](#)
- [85] Bolei Zhou, Hang Zhao, Xavier Puig, Tete Xiao, Sanja Fidler, Adela Barriuso, and Antonio Torralba. Semantic understanding of scenes through the ade20k dataset. *International Journal of Computer Vision*, 127(3):302–321, 2019. [6](#)

OCH3R: Object-Centric Holistic 3D Reconstruction

Supplementary Material

1. More reconstruction qualitative results

Fig. 1 presents additional single-view reconstruction results, where we render each predicted object-centric scene from three held-out novel viewpoints per input image. Across diverse indoor scenes, OCH3R produces geometrically consistent reconstructions that maintain object shapes and relative spatial arrangements under large viewpoint changes.

2. Additional individual task results

2.1. Pose estimation

We compare our zero-shot pose estimation performance against state-of-the-art methods. As shown in Tab. 1, OCH3R achieves consistently strong results on standard accuracy metrics (accuracy within 10 cm, within 10° , and under the joint $10^\circ/10$ cm threshold) across multiple datasets, reflecting the effectiveness of our NOCS-based pose estimation formulation. The advantage stems from jointly reasoning about depth, semantics, and canonical correspondences, which provides strong geometric and semantic cues even under distribution shift.

In addition to the quantitative comparison, we also include qualitative visualization on held-out test data in Fig. 2. These examples highlight that OCH3R produces clean, well-aligned 6D poses even in cluttered or partially occluded scenarios.

2.2. Full quantitative results for depth estimation

Due to space constraints, the main paper reports only δ_1 , AbsRel, and RMSE for monocular depth evaluation. For completeness, Tab. 2–Tab. 6 provide the full set of standard depth metrics (δ_1 , δ_2 , δ_3 , AbsRel, \log_{10} , RMSE, RMSE_{\log} , SILog) for all methods and datasets. The additional metrics confirm the trends observed in the main paper: OCH3R remains highly competitive, typically achieving the best or second-best performance across datasets and metrics.

3. Network and training details

3.1. Network architecture

Our architecture is inspired by VGGT [17] and builds on the DINOv2 ViT-L/14 [12] patch embedding as the backbone initialization. The input image is split into non-overlapping 14×14 patches, and each patch is linearly projected into a token. The resulting token sequence is then processed by a 42-layer transformer encoder with an embedding dimension of 1024 and 16 attention heads.

We employ four lightweight DPT-style [14] decoder heads for dense per-pixel prediction, together with a separate global camera head:

- **Semantic Head:** Consumes multi-scale encoder features and fuses them into a full-resolution feature map using lateral skips and convolutional fusion. A small projection MLP (hidden dimension 2048) maps these features to 512-dimensional per-pixel embeddings that live in the same space as CLIP text embeddings. During training, we compute cosine similarities between pixel embeddings and a set of CLIP text embeddings and use them as logits for an open-vocabulary semantic segmentation loss.
- **Depth Head:** Shares the same DPT-style fusion as the semantic head but outputs a single-channel canonical inverse-depth map $\hat{C}_{u,v}$. Following DepthPro-style canonicalization, we supervise \hat{C} via $C = f_w / (W \cdot d)$, where f_w is the horizontal focal length in pixels, W is the image width, and d is metric depth. At inference time, we recover metric depth by combining \hat{C} with the focal length derived from the predicted field-of-view.
- **NOCS Head:** Predicts per-pixel NOCS maps, i.e., 3D coordinates in a category-level canonical unit cube with consistent orientation and scale [16]. To better handle the multi-modality caused by object symmetries, we adopt a mixed classification–regression “bin-and-delta” parameterization: each of the X , Y , and Z coordinates is discretized into 64 uniform bins over $[0, 1]$, and the network jointly predicts a 64-way categorical distribution over bins together with a continuous offset from the chosen bin center. Prior work in NOCS-based reconstruction and category-level pose estimation has shown that discretizing continuous coordinates into bins provides greater robustness than direct L_2 regression under symmetric ambiguities [4, 16, 18]. Our formulation aligns with this strategy and follows the broader “bin-and-delta” design widely adopted in 3D pose estimation [8, 9].
- **Gaussian Head:** Implements our feed-forward 3D Gaussian predictor and is split into two sub-heads that share the same DPT-style multi-scale features but use a learnable upsampler (PixelShuffle or ConvTranspose-based) instead of simple bilinear interpolation to avoid over-smoothing structured parameters. The *geometry* sub-head predicts, for each pixel and for each of $k=2$ Gaussians, an off-ray offset $\Delta_{u,v}^{(i)} \in \mathbb{R}^3$ in camera space; adding this to the back-projected 3D point $\hat{\mathbf{p}}_{u,v}$ yields the Gaussian means $\mu_{u,v}^{(i)}$ in the camera frame. The *appearance/shape* sub-head predicts the remaining parameters in the canonical frame: log-scales (3 dims), a unit quaternion (4



Figure 1. **Additional object-centric reconstruction results.** Each row corresponds to one input image (left, not shown here), and we render three novel views of the reconstructed scene from different camera poses. OCH3R recovers coherent multi-object geometry that remains stable under large viewpoint changes.

Model	PACE			OMNI			YCB-V			HOPE			NOCS real		
	10cm \uparrow	10 $^\circ$ \uparrow	10 $^\circ$ 10cm \uparrow	10cm \uparrow	10 $^\circ$ \uparrow	10 $^\circ$ 10cm \uparrow	10cm \uparrow	10 $^\circ$ \uparrow	10 $^\circ$ 10cm \uparrow	10cm \uparrow	10 $^\circ$ \uparrow	10 $^\circ$ 10cm \uparrow	10cm \uparrow	10 $^\circ$ \uparrow	10 $^\circ$ 10cm \uparrow
AG-Pose [10]	44.2	<u>15.1</u>	<u>8.6</u>	0.0	<u>0.1</u>	0.0	0.0	16.2	0.0	<u>38.8</u>	<u>25.7</u>	<u>9.7</u>	48.7	<u>68.5</u>	30.1
SecondPose [3]	40.7	14.6	8.4	0.0	<u>0.1</u>	0.0	0.0	12.5	0.0	38.6	23.6	8.4	51.2	58.9	<u>31.6</u>
MonoDiff9D [11]	29.9	7.3	3.5	0.0	<u>0.1</u>	0.0	0.0	7.9	0.0	17.4	18.3	1.4	41.0	56.3	25.7
OCH3R (ours)	<u>41.8</u>	25.9	14.0	0.2	3.4	0.0	0.7	<u>15.9</u>	0.0	48.3	28.5	11.1	<u>49.6</u>	70.7	33.3

Table 1. Zero-shot 6D pose estimation results. Metrics: percentage of predictions within 10cm, within 10 $^\circ$, and within both.

dims) that defines the Gaussian orientation, opacity $\alpha_{u,v}^{(i)}$ (scalar), and RGB Spherical Harmonics coefficients of degree 0 (3 dims per Gaussian). We concatenate all parameters for the k Gaussians at each pixel into a single output tensor. Following NoPoSplat-style designs, this head also receives a shallow RGB shortcut to better preserve fine texture details in the predicted Gaussian colors.

- **Camera Head:** In addition to the dense heads, we attach a global camera head that follows the VGGT formulation. A learnable camera token is appended to the patch tokens and processed by a small stack of transformer blocks with adaptive layer-norm modulation and iterative refinement. A linear projection from the final camera token regresses the horizontal and vertical field-of-view angles ($\hat{\theta}_w, \hat{\theta}_h$) of the input image. These angles are converted into focal lengths via $f_w = \frac{W}{2 \tan(\hat{\theta}_w/2)}$ and $f_h = \frac{H}{2 \tan(\hat{\theta}_h/2)}$, which define the intrinsics matrix K used by our depth, NOCS, and Gaussian heads.

3.2. Training time and learning rate

We implement our model in PyTorch using PyTorch Lightning. Our model contains 1.4B parameters. Training is performed on 32 NVIDIA H100 GPUs (4 nodes \times 8 GPUs) for 30 epochs. The effective batch size is 64 (2 per GPU). We use the AdamW optimizer with a weight decay of 0.05. The learning rate is set to 1.25×10^{-4} with a linear warmup for the first 5% of steps, followed by a cosine decay schedule to a minimum of 1×10^{-6} .

3.3. Data augmentation

During training, we resize all images to a fixed width of 518. Following VGGT, we randomly crop the image with different aspect ratios ranging from 0.33 to 1. We apply data augmentation to enhance diversity, specifically utilizing random color jittering with a probability of 0.9 (adjusting brightness, contrast, and saturation by a factor of 0.5, and hue by 0.1), followed by random grayscale conversion with a probability of 0.05. We do not use horizontal flipping

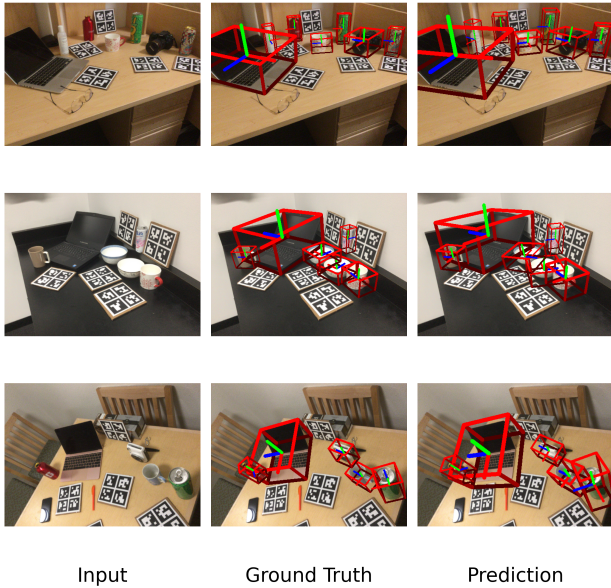


Figure 2. **Qualitative results for monocular pose estimation.** Our method is able to simultaneously predict the SIM(3) pose of all objects in the image.

to maintain consistency in the NOCS coordinate system.

3.4. Homoscedastic uncertainty weighting

We jointly optimize all tasks (depth, semantics, NOCS, Gaussian reconstruction, and camera FOV) using homoscedastic uncertainty weighting [7]. Concretely, let $\mathcal{L}_{\text{depth}}, \mathcal{L}_{\text{sem}}, \mathcal{L}_{\text{nocs}}, \mathcal{L}_{\text{css}}, \mathcal{L}_{\text{cam}}$ denote the per-task losses defined in Sec. 4 of the main paper. We associate each task t with a learnable log-variance parameter $s_t \in \mathbb{R}$, which is shared across all training examples and does not depend on the input (i.e., it models homoscedastic, task-specific observation noise). The total loss is

$$\mathcal{L}_{\text{total}} = \sum_{t \in \{\text{depth, sem, nocs, css, cam}\}} (\exp(-s_t) \mathcal{L}_t + s_t), \quad (1)$$

which is equivalent (up to constants) to the maximum-likelihood formulation in [7]. This parameterization guarantees positive effective weights $\exp(-s_t)$ and allows the model to automatically balance the relative importance of each task, avoiding manual tuning of heuristic loss coefficients while remaining stable throughout training.

4. Dataset details

4.1. Labeling and alignment

For semantic segmentation, we curated a unified vocabulary of 234 everyday object categories tailored specifically

for our training setup. Rather than directly adopting the category sets from PACE [20], Omni6DPose [22], GSO [5], and HyperSim [15], we consolidated and cleaned their ontologies, removed redundancies, harmonized naming conventions, and added missing but frequently observed items. This ensured comprehensive coverage of objects across all four datasets while maintaining a clean, consistent taxonomy suitable for multi-task training. The full vocabulary used for training is listed in Tab. 10. We use the pre-trained CLIP text encoder to obtain a 512-dimensional embedding for each category name.

For 3D alignment, we standardize object geometry and pose across heterogeneous sources to enable consistent supervision. PACE and Omni6DPose provide canonical 6D object poses out of the box. For GSO and HyperSim, however, we perform an additional normalization and alignment step: we center each asset, scale it to a unit cube following the NOCS convention, and manually correct orientation inconsistencies that arise due to varying dataset conventions and asset preparation pipelines. This careful consolidation produces a coherent canonical frame across all datasets, allowing us to supervise the NOCS head and the canonical-space Gaussian predictions under a uniform geometric definition.

4.2. Dataset Statistics

Our training corpus combines 50,000 frames from the PACE-Sim training split, 367,786 frames from the Omni6DPose SOPE.train split, 452,494 rendered views from Google Scanned Objects (GSO), and 50,319 frames from the HyperSim training split, for a total of 920,599 training images. For evaluation, we use 43,410 frames from the PACE test split, 332,359 frames from the Omni6DPose ROPE.test split, 2,949 keyframes from the YCB-V test_keyframe split, 50 validation images from HOPE, and 276 images from the NOCS-Real test split. Fig. 3 shows representative examples from each training and test dataset.

5. Ablation

5.1. Multi-task learning ablation on PACE

In Sec. 6.3 of the main paper we ablate the unified four-head design by removing one prediction head at a time (semantics, depth, NOCS, Gaussians). Tab. 7 shows full results on the PACE validation split. We report depth accuracy δ_1 (higher is better), pose accuracy under the joint $10^\circ/10$ cm criterion $A_{10^\circ/10\text{cm}}$, and Gaussian reconstruction PSNR (dB) in canonical space.

The full model with all four heads attains the best performance across all three metrics, indicating that the joint training objective provides a strong inductive bias for both geometry and semantics. Removing the semantic head

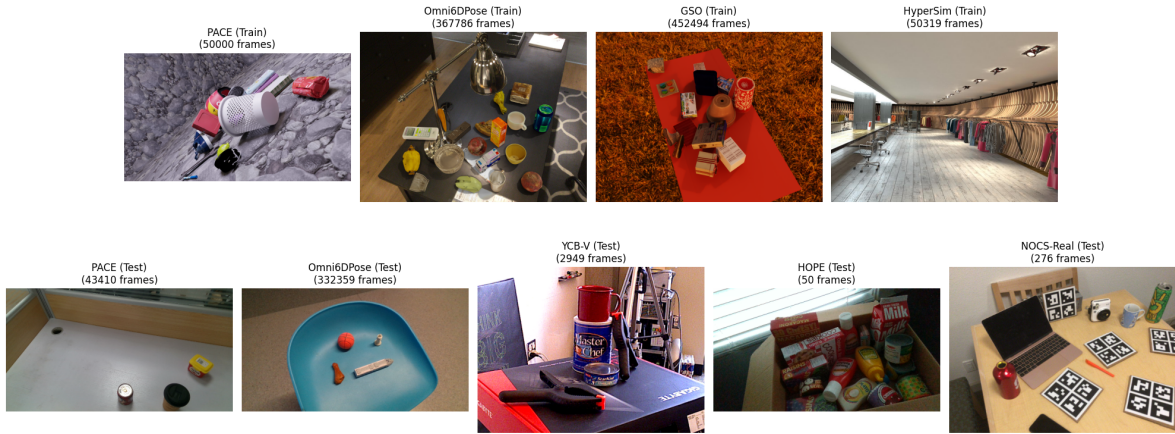


Figure 3. **Training and test datasets.** Representative RGB images from the four training datasets (PACE, Omni6DPose, GSO, HyperSim; top row) and five test datasets (PACE, Omni6DPose, YCB-V, HOPE, NOCS-Real; bottom row).

leads to the largest drop in pose and PSNR, suggesting that semantic embeddings are particularly important for stabilizing pose estimation and Gaussian reconstruction. Dropping the depth head also degrades pose and PSNR, showing that metric depth supervision benefits downstream 6D pose and canonical-space reconstruction even when depth is not evaluated directly. Omitting the NOCS head harms both depth and PSNR, highlighting the role of canonical coordinates in regularizing the 3D layout. Finally, training without the Gaussian head slightly reduces depth and pose accuracy, indicating that the reconstruction loss feeds back into the shared backbone and improves the other tasks as well.

Model	$\delta_1 \uparrow$	$A_{10^\circ/10\text{cm}} \uparrow$	PSNR (dB) \uparrow
Full (all heads)	95.6	14.2	28.6
w/o Sem. head	91.1	8.9	24.0
w/o Depth head	–	11.6	27.8
w/o NOCS head	88.2	–	25.2
w/o Gauss head	95.2	13.5	–

Table 7. **Multi-task ablation** on PACE (validation split). Depth (δ_1 , %), pose accuracy $A_{10^\circ/10\text{cm}}$ (%), and Gaussian PSNR (dB) when removing one prediction head at a time. For PSNR, we transform the predicted Gaussians into canonical space and render them using ground-truth instance information for all non-Gaussian quantities, so the metric isolates the effect of the Gaussian head.

5.2. Offset in camera space vs. direct canonical Gaussians

In Sec. 6.3 of the main paper we qualitatively compared our default camera-space offset parameterization of Gaussian means with a variant that predicts Gaussian parameters directly in the canonical frame, bypassing the offset-along-ray formulation. For completeness, we report quantitative

results of this ablation.

The **camera-space** model is our default OCH3R: each pixel first predicts metric depth and a per-pixel 3D point along the camera ray, and the Gaussian means are obtained by adding a learned off-ray offset in camera space before being transformed into canonical space via the object SIM(3) pose. The **direct canonical** ablation instead predicts Gaussian means directly in the canonical frame from the same backbone features; these Gaussians are rendered in canonical space with CSS, but no geometric constraint ties a given pixel to a particular region of the object.

We train both variants from scratch with identical hyperparameters. For geometry, we follow the evaluation protocol of Sec. 6.1 and report Chamfer Distance and F-1@0.1 between the reconstructed and ground-truth meshes. For appearance, we measure CLIP similarity between canonical renderings of the predicted and ground-truth objects, and additionally report PSNR (in dB) computed over the same set of canonical views used for Canonical-Space Supervision.

Model	CD \downarrow	F-1@0.1 \uparrow	CLIP \uparrow	PSNR \uparrow (dB)
Camera-space offsets (ours)	0.18	45.90	83.41	27.57
Direct canonical Gaussians	0.35	15.10	79.20	23.65

Table 8. **Camera-space offsets vs. direct canonical Gaussians** on PACE (validation split). Predicting Gaussian means as camera-space offsets along rays yields substantially better geometry and appearance than regressing Gaussians directly in canonical space.

On PACE (validation split), removing the camera-ray scaffold causes the network to converge to a degenerate solution: average Chamfer Distance increases from 0.18 to 0.35, and F-1@0.1 falls from 45.90 to 15.10. Despite this

geometric collapse, the drop in CLIP similarity is comparatively modest (from 83.4 to 79.2), indicating that the direct-canonical model still matches coarse color and texture but fails to organize Gaussians into a coherent 3D shape. The strong PSNR gap in canonical space (27.57 dB vs. 23.65 dB) confirms that camera-space offsets provide a crucial inductive bias: they tie each pixel’s Gaussians to a geometrically meaningful 3D location, allowing CSS to assemble accurate and amodally complete reconstructions.

5.3. Effect of model scale and architecture

As discussed in the main paper, our formulation, particularly the multi-task learning setup and Canonical-Space Supervision, is largely orthogonal to the choice of dense backbone. To quantify this, we evaluate three transformer backbones with different depths (12, 32, and 48 layers) as well as a U-Net whose parameter count roughly matches the 32-layer ViT. All models share the same DINOv2 [12] image encoder and task heads and are trained on the same data. Tab. 9 reports results on the PACE validation split, using the 3D reconstruction metrics from the main paper: Chamfer Distance (CD), F-1@0.1, and CLIP similarity between rendered predictions and ground-truth images, along with average inference time per image.

Model	CD↓	F-1↑	CLIP↑	Time / img (s)↓
ViT-12	0.30	28.93	81.05	0.45
U-Net	0.29	31.11	81.88	0.52
ViT-32	0.20	40.05	82.36	0.59
ViT-48 (ours)	0.18	45.90	83.41	0.70

Table 9. **Model scale and architecture ablation** on PACE (validation split). CD is Chamfer Distance (lower is better), F-1 is evaluated at 0.1, and CLIP is image-space similarity (higher is better).

Across all metrics, performance scales smoothly with model capacity: the smallest ViT-12 backbone already yields strong reconstructions, while the 48-layer ViT further reduces CD and improves F-1 and CLIP, at the cost of slightly higher runtime. The U-Net remains competitive with the transformer models, supporting our claim that the OCH3R pipeline transfers across dense architectures while benefiting from additional capacity.

6. Failure cases and limitations

Despite its strong performance, OCH3R has several limitations.

- **Mirror and glass:** Highly reflective or transparent surfaces remain challenging for our depth and NOCS estimators, often producing unstable geometry and inaccurate poses because appearance cues are inconsistent with the underlying 3D structure.

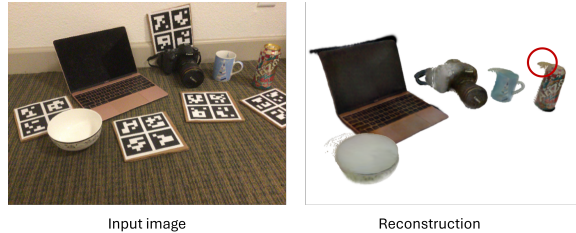


Figure 4. **Depth-Gaussian coupling.** When the predicted depth is biased, the corresponding Gaussians (circled) are consistently displaced from the true object surface, illustrating the coupling between depth accuracy and 3D reconstruction quality.

- **Depth-Gaussian coupling:** As illustrated in Fig. 4, Gaussian means inherit their initial placement from the predicted depth before applying the learned off-ray offset. Small, structured depth inaccuracies (e.g., at thin object boundaries) can therefore propagate into mild Gaussian misalignment. This coupling arises only when depth deviates systematically and does not impact most objects.
- **Back-side blur:** Because OCH3R relies on a single feed-forward pass without iterative probabilistic refinement (e.g., flow matching or diffusion), rarely observed back surfaces may appear slightly over-smoothed. These cases occur primarily for objects with unusual topology or very uncommon categories where canonical priors are weak (e.g., highly concave shapes, irregular sculptures).

Model	δ_1 (%) \uparrow	δ_2 (%) \uparrow	δ_3 (%) \uparrow	AbsRel \downarrow	\log_{10} \downarrow	RMSE \downarrow	RMSE $_{\log}$ \downarrow	SILog \downarrow
NeWCRFs [21]	17.00	44.56	72.73	0.7356	0.2208	0.5308	0.5835	0.2952
ZoeDepth [1]	8.20	31.99	62.11	0.8508	0.2530	0.6146	0.6366	0.2602
Metric3D V2 [6]	1.32	13.42	55.34	0.4695	0.2835	0.3995	0.6817	0.1971
Depth Anything V2 [19]	13.07	37.82	70.65	0.7373	0.2274	0.5906	0.5789	0.2798
Depth Pro [2]	33.63	61.60	81.87	0.5603	0.1728	0.5610	0.4989	0.3523
VGGT [17]	<u>55.58</u>	<u>91.24</u>	<u>99.20</u>	<u>0.2415</u>	<u>0.0961</u>	<u>0.2096</u>	<u>0.2699</u>	0.2607
UniDepth V2 [13]	35.05	63.91	83.87	0.5076	0.1667	0.4820	0.4783	0.3896
OCH3R (ours)	94.82	99.60	99.88	0.0834	0.0368	0.1039	0.1168	0.1142

Table 2. Full monocular depth estimation results on PACE (test split). δ_1 , δ_2 , and δ_3 are reported in percentage. All models are evaluated using their largest available variant.

Model	δ_1 (%) \uparrow	δ_2 (%) \uparrow	δ_3 (%) \uparrow	AbsRel \downarrow	\log_{10} \downarrow	RMSE \downarrow	RMSE $_{\log}$ \downarrow	SILog \downarrow
NeWCRFs [21]	21.41	50.42	78.75	0.6432	0.2015	0.9934	0.5416	0.3429
ZoeDepth [1]	20.73	54.47	84.47	0.5794	0.1881	0.9406	0.4961	0.2825
Metric3D V2 [6]	73.73	94.56	98.85	0.1788	0.0740	<u>0.7963</u>	0.2371	0.2349
Depth Anything V2 [19]	5.83	27.10	61.84	0.9009	0.2651	1.1728	0.6641	0.2823
Depth Pro [2]	<u>57.37</u>	86.69	96.35	0.2742	0.1023	0.7940	0.3108	0.2789
VGGT [17]	57.14	90.28	97.98	<u>0.2272</u>	0.0992	1.0365	0.3050	0.3017
UniDepth V2 [13]	22.80	50.17	73.47	0.7221	0.2155	1.1007	0.5997	0.4303
OCH3R (ours)	42.77	<u>91.76</u>	99.23	0.2900	<u>0.0812</u>	0.8042	<u>0.2743</u>	0.2897

Table 3. Full monocular depth estimation results on OMNI (Rope split). δ_1 , δ_2 , and δ_3 are reported in percentage. All models are evaluated using their largest available variant.

Model	δ_1 (%) \uparrow	δ_2 (%) \uparrow	δ_3 (%) \uparrow	AbsRel \downarrow	\log_{10} \downarrow	RMSE \downarrow	RMSE $_{\log}$ \downarrow	SILog \downarrow
NeWCRFs [21]	52.71	91.70	99.13	0.2740	0.1004	0.2699	0.2759	0.1687
ZoeDepth [1]	52.84	90.67	98.85	0.2704	0.0986	0.2750	0.2764	0.1727
Metric3D V2 [6]	15.44	84.96	<u>99.82</u>	0.2791	0.1443	0.2538	0.3486	0.1107
Depth Anything V2 [19]	50.74	97.23	99.62	<u>0.1899</u>	0.0929	0.2029	<u>0.2532</u>	0.1709
Depth Pro [2]	49.04	94.40	99.65	0.2078	0.1000	0.2148	0.2714	0.2212
VGGT [17]	<u>63.88</u>	87.46	97.93	0.1822	<u>0.0900</u>	0.2131	0.2742	0.2468
UniDepth V2 [13]	32.70	80.73	99.43	0.2548	0.1315	0.2499	0.3416	0.1783
OCH3R (ours)	69.96	<u>95.34</u>	99.87	0.1933	0.0864	<u>0.2044</u>	0.2405	<u>0.1635</u>

Table 4. Full monocular depth estimation results on YCB-V. δ_1 , δ_2 , and δ_3 are reported in percentage. All models are evaluated using their largest available variant.

Model	δ_1 (%) \uparrow	δ_2 (%) \uparrow	δ_3 (%) \uparrow	AbsRel \downarrow	\log_{10} \downarrow	RMSE \downarrow	RMSE $_{\log}$ \downarrow	SILog \downarrow
NeWCRFs [21]	5.37	33.98	64.47	0.8073	0.2458	0.5029	0.6107	0.2335
ZoeDepth [1]	0.53	21.32	63.87	0.9814	0.2812	0.6055	0.6990	0.2667
Metric3D V2 [6]	0.01	24.72	91.66	0.4039	0.2274	0.2968	0.5364	0.1167
Depth Anything V2 [19]	0.07	0.24	49.05	1.0364	0.3055	0.6518	0.7147	0.1340
Depth Pro [2]	23.09	<u>82.05</u>	<u>99.79</u>	<u>0.4035</u>	<u>0.1437</u>	0.3013	<u>0.3581</u>	0.1437
VGGT [17]	<u>37.17</u>	72.29	84.27	0.4313	0.1438	<u>0.2844</u>	0.4043	0.2439
UniDepth V2 [13]	8.63	47.83	84.67	0.7622	0.2190	0.6830	0.5931	0.3173
OCH3R (ours)	61.36	98.82	99.91	0.2192	0.0852	0.1812	0.2351	<u>0.1296</u>

Table 5. Full monocular depth estimation results on HOPE. δ_1 , δ_2 , and δ_3 are reported in percentage. All models are evaluated using their largest available variant.

Model	δ_1 (%) \uparrow	δ_2 (%) \uparrow	δ_3 (%) \uparrow	AbsRel \downarrow	\log_{10} \downarrow	RMSE \downarrow	RMSE $_{\log}$ \downarrow	SILog \downarrow
NeWCRFs [21]	36.00	86.70	99.40	0.3352	0.1211	0.3586	0.3133	0.1503
ZoeDepth [1]	34.08	66.71	93.76	0.4399	0.1492	0.5275	0.3993	0.2090
Metric3D V2 [6]	8.50	60.26	99.66	0.3273	0.1747	0.3571	0.4160	<u>0.1068</u>
Depth Anything V2 [19]	2.44	69.03	90.58	0.5507	0.1851	0.6088	0.4533	0.1554
Depth Pro [2]	81.58	<u>99.91</u>	<u>99.99</u>	0.1370	0.0545	0.1831	0.1576	0.1322
VGGT [17]	<u>92.26</u>	99.66	99.98	<u>0.0965</u>	<u>0.0438</u>	<u>0.1394</u>	<u>0.1278</u>	0.1200
UniDepth V2 [13]	78.92	97.17	99.16	0.1778	0.0678	0.2366	0.1979	0.1339
OCH3R (ours)	98.43	99.97	100.00	0.0923	0.0378	0.1066	0.1051	0.0704

Table 6. Full monocular depth estimation results on NOCS (real split). δ_1 , δ_2 , and δ_3 are reported in percentage. All models are evaluated using their largest available variant.

adhesive_tape_roll	backpack	bag	ball	bamboo_mat
bamboo_shoots	banana	bannister	barrel	basket_container
bathub	battery	bed	bell	belt
blinds	board_game	book	bookshelf	bottle
bowl	box	bread	brush	building_blocks
bumbag	burger	cabinet	cable	cake
calculator	camera	can	candle	candy
carrot	carton_beverage_container	ceiling	chair	chess
chicken_leg	chili	chinese_chess	chip_can	clip
clock	clothes	coconut	column	conch
corn	counter	cradle	cucumber	cup
curtain	cutter	desk	desk_caddy	dice
dinosaur	dishwasher	doll	donut	door
dresser	dumbbell	dumpling	dustpan	egg
egg_tart	electronic_device	eraser	fan	figure
fire_extinguisher	fireplace	flash_light	floor	floormat
flower_pot	flute	fork	frisbee	garlic
glasses	glasses_case	gloves	guitar	hair_dryer
hair_styling_tool	hairpin	hammer	handbag	hat
headset	helmet	hook	hot_dog	insole
instant_noodle_cup	kettle	keyboard	kitchen_utensil	knife
lamp	laptop	laundry_detergent	lemon	lens
light	lipstick	magnet	magnifying_glass	mango
mangosteen	marker	medicine_bottle	melon	mirror
monitor	mooncake	mosaic_tiles	mouse	mug
nightstand	notebook	onion	orange	other
otherfurniture	otherprop	otherstructure	oven	pad
painting	pan	paper	peach	pear
pen	pencil	pencil_case	person	pillow
pineapple	pitaya	pitcher	pizza	plate
plug	plush_toy	pomegranate	pot	power_strip
projector	pumpkin	radiator	razor	refrigerator
remote_control	ricecooker	rubik_cube	sausage	scissor
sculpture	shelves	shoe	shower	showercurtain
shrimp	sink	slipper	snack	soap
soap_dish	sofa	spanner	speaker	sponge
spoon	squeegee	stairs	starfish	stool
stove	suitcase	sweet_potato	sword_bean	table
table_tennis_bat	tableware_set	tape_measure	teapot	television
timer	tissue	toaster	toilet	toiletries
tomato	tool	toolkit	toothbrush	towel
toy	toy_animals	toy_blocks	toy_boat	toy_bus
toy_car	toy_food	toy_furniture_set	toy_motorcycle	toy_plane
toy_plant	toy_stacking_rings	toy_train	toy_train_track	toy_truck
umbrella	usb_drive	vase	vegetable	waffle
wall	wallet	watch	watermelon	whistle
whiteboard	window	wine_glass	wristband	

Table 10. List of all 234 semantic categories used in our method.

References

- [1] Shariq Farooq Bhat, Reiner Birkel, Diana Wofk, Peter Wonka, and Matthias Müller. Zoedepth: Zero-shot transfer by combining relative and metric depth, 2023. 6
- [2] Aleksei Bochkovskii, Amaël Delaunoy, Hugo Germain, Marcel Santos, Yichao Zhou, Stephan R. Richter, and Vladlen Koltun. Depth pro: Sharp monocular metric depth in less than a second, 2025. 6
- [3] Yamei Chen, Yan Di, Guangyao Zhai, Fabian Manhardt, Chenyangguang Zhang, Ruida Zhang, Federico Tombari, Nassir Navab, and Benjamin Busam. Secondpose: Se(3)-consistent dual-stream feature fusion for category-level pose estimation. In *Proceedings of the IEEE/CVF Conference on Computer Vision and Pattern Recognition (CVPR)*, pages 9959–9969, 2024. 2
- [4] Cheng Chi and Shuran Song. Garmentnets: Category-level pose estimation for garments via canonical space shape completion, 2021. 1
- [5] Laura Downs, Anthony Francis, Nate Koenig, Brandon Kinman, Ryan Hickman, Krista Reymann, Thomas B. McHugh, and Vincent Vanhoucke. Google scanned objects: A high-quality dataset of 3d scanned household items, 2022. 3
- [6] Mu Hu, Wei Yin, Chi Zhang, Zhipeng Cai, Xiaoxiao Long, Hao Chen, Kaixuan Wang, Gang Yu, Chunhua Shen, and Shaojie Shen. Metric3d v2: A versatile monocular geometric foundation model for zero-shot metric depth and surface normal estimation. *IEEE Transactions on Pattern Analysis and Machine Intelligence*, 46(12):10579–10596, 2024. 6
- [7] Alex Kendall, Yarin Gal, and Roberto Cipolla. Multi-task learning using uncertainty to weigh losses for scene geometry and semantics, 2018. 3
- [8] Jake Levinson, Carlos Esteves, Kefan Chen, Noah Snaveley, Angjoo Kanazawa, Afshin Rostamizadeh, and Ameet Makadia. An analysis of svd for deep rotation estimation, 2020. 1
- [9] Chi Li, Jin Bai, and Gregory D. Hager. A unified framework for multi-view multi-class object pose estimation, 2018. 1
- [10] Xiao Lin, Wenfei Yang, Yuan Gao, and Tianzhu Zhang. Instance-adaptive and geometric-aware keypoint learning for category-level 6d object pose estimation. In *Proceedings of the IEEE/CVF Conference on Computer Vision and Pattern Recognition*, pages 21040–21049, 2024. 2
- [11] Jian Liu, Wei Sun, Hui Yang, Jin Zheng, Zichen Geng, Hossein Rahmani, and Ajmal Mian. Monodiff9d: Monocular category-level 9d object pose estimation via diffusion model. In *IEEE International Conference on Robotics and Automation (ICRA)*, 2025. 2
- [12] Maxime Oquab, Timothée Darcet, Théo Moutakanni, Huy Vo, Marc Szafraniec, Vasil Khalidov, Pierre Fernandez, Daniel Haziza, Francisco Massa, Alaaeldin El-Nouby, Mahmoud Assran, Nicolas Ballas, Wojciech Galuba, Russell Howes, Po-Yao Huang, Shang-Wen Li, Ishan Misra, Michael Rabbat, Vasu Sharma, Gabriel Synnaeve, Hu Xu, Hervé Jegou, Julien Mairal, Patrick Labatut, Armand Joulin, and Piotr Bojanowski. Dinov2: Learning robust visual features without supervision, 2024. 1, 5
- [13] Luigi Piccinelli, Christos Sakaridis, Yung-Hsu Yang, Mattia Segu, Siyuan Li, Wim Abbeels, and Luc Van Gool. Unidepthv2: Universal monocular metric depth estimation made simpler, 2025. 6
- [14] René Ranftl, Alexey Bochkovskiy, and Vladlen Koltun. Vision transformers for dense prediction, 2021. 1
- [15] Mike Roberts, Jason Ramapuram, Anurag Ranjan, Atulit Kumar, Miguel Angel Bautista, Nathan Paczan, Russ Webb, and Joshua M. Susskind. Hypersim: A photorealistic synthetic dataset for holistic indoor scene understanding, 2021. 3
- [16] He Wang, Srinath Sridhar, Jingwei Huang, Julien Valentin, Shuran Song, and Leonidas J Guibas. Normalized object coordinate space for category-level 6d object pose and size estimation. In *Proceedings of the IEEE/CVF conference on computer vision and pattern recognition*, pages 2642–2651, 2019. 1
- [17] Jianyuan Wang, Minghao Chen, Nikita Karaev, Andrea Vedaldi, Christian Rupprecht, and David Novotny. Vgg: Visual geometry grounded transformer, 2025. 1, 6
- [18] Han Xue, Wenqiang Xu, Jieyi Zhang, Tutian Tang, Yutong Li, Wenxin Du, Ruolin Ye, and Cewu Lu. Garmenttracking: Category-level garment pose tracking, 2025. 1
- [19] Lihe Yang, Bingyi Kang, Zilong Huang, Zhen Zhao, Xiaogang Xu, Jiashi Feng, and Hengshuang Zhao. Depth anything v2, 2024. 6
- [20] Yang You, Kai Xiong, Zhening Yang, Zhengxiang Huang, Junwei Zhou, Ruoxi Shi, Zhou Fang, Adam W. Harley, Leonidas Guibas, and Cewu Lu. Pace: A large-scale dataset with pose annotations in cluttered environments, 2024. 3
- [21] Weihao Yuan, Xiaodong Gu, Zuozhuo Dai, Siyu Zhu, and Ping Tan. New crfs: Neural window fully-connected crfs for monocular depth estimation, 2022. 6
- [22] Jiyao Zhang, Weiyao Huang, Bo Peng, Mingdong Wu, Fei Hu, Zijian Chen, Bo Zhao, and Hao Dong. Omni6dpose: A benchmark and model for universal 6d object pose estimation and tracking, 2024. 3